Rigorous Coupling of Geomechanics and Multiphase Flow with Strong Capillarity

J. Kim, SPE, Lawrence Berkeley National Laboratory; **H.A. Tchelepi,** SPE, Stanford University; and **R. Juanes,** Massachusetts Institute of Technology

Summary

We study sequential formulations for coupled multiphase flow and reservoir geomechanics. First, we identify the proper definition of effective stress in multiphase-fluid systems. Although the average pore-pressure $\overline{p}$—defined as the sum of the product of saturation and pressure of all the fluid phases that occupy the pore space—is commonly used to describe multiphase-fluid flow in deformable porous media, it can be shown that the "equivalent" pore pressure p_E—defined as $\overline{p}$ minus the interfacial energy—is the appropriate quantity (Coussy 2004). We show, by means of a fully implicit analysis of the system, that only the equivalent pore pressure p_E leads to a continuum problem that is thermodynamically stable (thus, numerical discretizations on the basis of the average pore pressure $\overline{p}$ cannot render unconditionally stable and convergent schemes). We then study the convergence and stability properties of sequential-implicit coupling strategies. We show that the stability and convergence properties of sequential-implicit coupling strategies for single-phase flow carry over for multiphase systems if the equivalent pore pressure p_E is used. Specifically, the undrained and fixed-stress schemes are unconditionally stable, and the fixed-stress split is superior to the undrained approach in terms of convergence rate. The findings from stability theory are verified by use of nonlinear simulations of two-phase flow in deformable reservoirs.

Introduction

The coupling of mechanical deformation and multiphase-fluid flow in porous media is central to many natural and man-made systems in civil, environmental, and petroleum engineering. For example, in civil engineering, soils can shrink as a result of water evaporation, because vaporization decreases the fluid pore pressure and results in compressive effective stresses (Coussy et al. 1998); frost heaving caused by phase changes of water can lead to an increase in the fluid pore pressure causing tensile effective stresses; and porous materials such as concrete can suffer from tensile failure and cracking (Coussy 2005).

In environmental engineering, the disposal of nuclear waste in the subsurface increases the temperature of the geological formation, which can lead to changes in the mechanical equilibrium and the hydrological properties (e.g., permeability or porosity). In carbon dioxide (CO_2) sequestration operations, injection of CO_2 underground will cause an increase in pore pressure, and this will limit storage capacity (Szulczewski et al. 2012), and may lead to induced seismicity (Cappa and Rutqvist 2011) and potentially affect caprock integrity and cause leakage of CO_2 (Chiaramonte et al. 2008; Rutqvist et al. 2008; Morris et al. 2011). For geothermal fields, injection of cold water and production of hot water can lead to significant geomechanical deformation.

In petroleum engineering, the oil industry deals with a wide range of problems that involve geomechanical deformation, including the stability of boreholes and surface facilities, hydraulic fracturing, reservoir compaction, sand production, and heavy oil and gas-hydrate recovery (e.g., Merle et al. 1976; Kosloff et al. 1980; Lewis and Schrefler 1998; Bagheri and Settari 2008; Freeman et al. 2009; Jain and Juanes 2009; Rutqvist and Moridis 2009; Holtzman and Juanes 2011; Holtzman et al. 2012; Kim et al. 2012a, 2012b). These challenging engineering problems involve complex interactions between geomechanics, fluid flow, and heat transfer. Capillarity effects such as matrix suction play a critical role in unsaturated soil mechanics—for example, significantly affecting the material strength, fluid flow, subsurface deformation, and the effective-stress state (Maswoswe 1985; Josa et al. 1987; Josa 1988; Alonso et al. 1990; Fredlund and Rahardjo 1993a, 1993b; Olivella et al. 1996; Terzaghi et al. 1996; Khalili and Khabbaz 1998; Dangla et al. 2000; Mainguy et al. 2001; Mayor et al. 2007; Zhang et al. 2007; Nuth and Laloui 2008). In geotechnical engineering, civil engineering, or radioactive waste disposal problems, capillary pressures can experience magnitudes up to 0.2 MPa in sandy clay (Alonso et al. 1990), 1.0 MPa for clayey silt (Fredlund and Rahardjo 1993b), 20.0 MPa from the ventilation test in the Mont Terri underground laboratory (Mayor et al. 2007), 100 MPa for the Opalinus clay or clay barriers (Dangla et al. 2000; Zhang et al. 2007), and higher than 100 MPa for hardened cement or concrete samples (Mainguy et al. 2001).

Several authors have proposed constitutive relations to model coupled flow and mechanics (e.g., Biot 1941; Biot and Willis 1957; Geertsma 1957; Bishop 1959; Alonso et al. 1990; Fredlund and Rahardjo 1993b; Lewis and Sukirman 1993b; Coussy 1995; Lewis and Schrefler 1998; Coussy 2004; Borja 2006). Biot (1941), Geertsma (1957), and Biot and Willis (1957) developed the constitutive equations for single-phase flow of a slightly compressible fluid, and they proposed laboratory tests to determine the various coupling coefficients.

For multiphase flow, the definition of the effective stress is still controversial, and several constitutive models have been proposed. For example, Bishop (1959) proposed a formulation of effective stress in a water-air system by introducing a weighted suction term. The weighting of this term is determined through laboratory experiments, and depends on the type of geomaterial (Bishop and Donald 1961; Khalili and Khabbaz 1998). Alonso et al. (1990) introduced a constitutive model to capture suction effects in poroplasticity. Nuth and Laloui (2008) reviewed and compared effective-stress models, classifying them into three types: independent-variable effective stresses, Category 1 effective stresses, and Category 2 effective stresses. In the independent-variable effective-stress approach, deformation is modeled by two independent state variables, such as total stress minus air pressure and suction (Alonso et al. 1990). The effective stress of Category 1 is expressed by the total stress minus air pressure and an additional term that is a function of suction, whereas that of Category 2 employs an additional term that is a function of suction and phase saturation. Among the three types of formulations, Nuth and Laloui (2008) conclude that effective stresses of Category 2 are the most advantageous and robust when dealing with saturated-unsaturated transitions, hysteresis effects, and hardening. The constitutive models proposed by Lewis and Schrefler (1998), Borja (2006), and Coussy (2004) all use effective stresses of Category 2. The model by Lewis and Sukirman (1993b) and Lewis and Schrefler (1998) provides explicit expressions of the physical quantities of interest (i.e., coefficients in the governing equations), which can be used in engineering applications. The model of Borja (2006), examining different definitions of the effective stress, shows that the coupling is thermodynamically

This paper (SPE 141268) was accepted for presentation at the SPE Reservoir Simulation Symposium, The Woodlands, Texas, USA, 21–23 February 2011, and revised for publication. Original manuscript received for review 12 December 2010. Revised manuscript received for review 1 May 2013. Paper peer approved 7 May 2013.

stable. However, Borja (2006) proposed experiments to determine the physical quantities, such as the bulk modulus, that are somewhat different from those proposed by Biot and Willis (1957). The models by Coussy (1995) and Coussy et al. (1998) provide thermodynamically consistent constitutive relations for more general cases, including large deformation and plasticity.

Two numerical solution strategies are commonly used for the solution of coupled flow–mechanics problems: fully implicit (monolithic) and sequential-implicit (staggered) methods. In the fully implicit method (FIM), one solves the coupled discrete nonlinear system of equations simultaneously, typically using the Newton-Raphson scheme (Lewis and Sukirman 1993a, 1993b; Sukirman and Lewis 1993; Pao et al. 2001; Gutierrez and Lewis 2002; Pao and Lewis 2002; Lewis et al. 2003; Li et al. 2005; Ferronato et al. 2010). FIM guarantees unconditional stability for a well-posed problem. In practice, the FIM approach is quite costly, in terms of both the effort required to develop a unified flow-mechanics code and the need for computational resources. In contrast, sequential approaches split the coupled problem into two subproblems—one for flow and one for mechanics—and the two problems are then solved in sequence. A sequential coupling strategy allows the integration of two separate simulation codes, each designed specifically for modeling either flow or mechanics. Although this flexibility is highly desirable, sequential schemes are advantageous for solving coupled flow–mechanics problems of practical interest only if their stability and convergence properties are competitive with those enjoyed by FIM.

Considerable effort has been invested in devising sequential-implicit methods with improved accuracy, stability, and convergence properties. For dynamic mechanics and single-phase-fluid (or heat) flow, Zienkiewicz et al. (1988) and Armero and Simo (1992, 1993) proposed an unconditionally stable scheme based on an undrained split of the flow and mechanics problems. Armero and Simo (1992) showed that the undrained split honors the dissipative character of the coupled flow–mechanics problem. Armero (1999) applied the undrained split to the coupled, quasistatic, single-phase-fluid flow and mechanics in the presence of finite deformation. Settari and Mourits (1994) proposed a sequential-implicit method, where the flow problem is solved first, followed by the mechanics problem. When the flow problem is solved first, the "rock compressibility" term can be used as a relaxation parameter to control the convergence rate of the overall coupled scheme (Settari and Mourits 1994, 1998; Mainguy and Longuemare 2002; Jean et al. 2007). Recently, Kim et al. (2011a, 2011b, 2011c) performed stability and convergence analyses of sequential-implicit solution strategies of coupled geomechanics and single-phase flow in porous media. They studied four coupling strategies: drained, undrained, fixed-strain, and fixed-stress. They concluded that the undrained and fixed-stress methods have superior stability properties compared with the drained and fixed-strain variants. They also showed that the fixed-stress coupling strategy leads to faster convergence rates compared with the undrained approach (Kim et al. 2011a).

In engineering practice, multiple fluid phases (water, oil, and/or gas) are often present in the pore space of the formation under consideration. Therefore, the primary objective of this work is to devise effective solution strategies for coupled flow and geomechanics problems when multiple fluid phases share the pore space. However, before we can turn our attention to coupling issues and efficient sequential (staggered) solution strategies, we first need to determine which definition of effective stress renders a well-posed continuum problem. Here, we show that the equivalent pore-pressure p_E, as defined by Coussy (2004), is the appropriate definition of pressure to be used when solving the coupled problem, and that the saturation-weighted pore-pressure $\overline{p}$ is not adequate, especially when capillarity is strong. Then, once the proper definition of pore pressure (i.e., p_E) in the governing equations and constitutive relations is identified, we perform a thorough analysis of the stability and convergence properties of sequential-implicit strategies for the solution of coupled geomechanics-flow problems in the presence of strong capillarity.

Mathematical Formulation

We use a classical continuum representation, where the fluids and the solid skeleton are viewed as overlapping continua. The governing equations for flow and mechanics are obtained from mass and linear-momentum balances, respectively. For multiphase flow, the mass-conservation equation is expressed as

$$\frac{\mathrm{d}m_J}{\mathrm{d}t} + \mathrm{Div}\,\boldsymbol{w}_J = (\rho f)_J, \quad \ldots\ldots\ldots\ldots\ldots\ldots\ldots\ldots (1)$$

where the subscript J denotes a particular fluid phase. Here, m is fluid mass per unit volume of porous medium, ρ is density, f is a volumetric source term, $\mathrm{Div}(\cdot)$ is the divergence operator, and $\boldsymbol{w}_J$ is the mass-flux of fluid phase J relative to the solid skeleton. The accumulation term, $\frac{\mathrm{d}m_J}{\mathrm{d}t}$, describes the time variation of fluid mass relative to the motion of the solid skeleton. From here on, we denote by $\mathrm{d}(\cdot)/\mathrm{d}t$ the change of a quantity $(\cdot)$ relative to the motion of the solid skeleton.

The volumetric flux of phase J, $\boldsymbol{v}_J = (\boldsymbol{w}/\rho_0)_J$, is given by Darcy's law as

$$\boldsymbol{v}_J = -\frac{1}{B_J}\frac{\boldsymbol{k}_{p,JK}}{\mu_J}(\mathbf{Grad}\,p_K - \rho_K \boldsymbol{g}), \quad \ldots\ldots\ldots\ldots\ldots (2)$$

where $\boldsymbol{k}_{p,JK}$ is the effective-permeability tensor in the presence of two fluid phases J and K, and μ_J and $B_J = (\rho_0/\rho)_J$ denote the viscosity and formation volume factor (normalized phase density) of fluid phase J, respectively (Aziz and Settari 1979). Double indices (e.g., K in Eq. 2) indicate summation. Typically in reservoir simulation, $\boldsymbol{k}_{p,JK}$ is split into an absolute permeability $\boldsymbol{k}_p$ and a relative permeability k^r_{JK}, which is expressed as $\boldsymbol{k}_{p,JK} = \boldsymbol{k}_p k^r_{JK}$, where $k^r_{JK} = 0$ if $J \neq K$.

Under the quasistatic assumption, the governing equation for mechanical equilibrium can be written as

$$\mathrm{Div}\,\boldsymbol{\sigma} + \rho_b \boldsymbol{g} = \mathbf{0}, \quad \ldots\ldots\ldots\ldots\ldots\ldots\ldots\ldots (3)$$

where $\boldsymbol{\sigma}$ is the Cauchy total-stress tensor, $\boldsymbol{g}$ denotes gravity, $\rho_b = \phi\rho_f + (1-\phi)\rho_s$ is bulk density, ρ_f is total fluid density, ρ_s is solid-phase density, and ϕ is the "true" porosity. The true porosity is defined as the ratio of the pore volume to the bulk volume in the deformed configuration. In this paper, we assume small deformation (i.e., the infinitesimal transformation is applicable), isotropic geomaterial, and isothermal conditions. On the basis of these assumptions, the changes in total stress and fluid pressure(s) are related to changes in strain and fluid content, as follows (Coussy 1995, 2004):

$$\delta\boldsymbol{\sigma} = \underbrace{\mathbf{C}_{dr} : (\delta\boldsymbol{\varepsilon} - \delta\boldsymbol{\varepsilon}_p)}_{\delta\sigma'} - b_J \delta p_J \mathbf{1}, \quad \ldots\ldots\ldots\ldots\ldots (4)$$

$$\delta p_J = M_{JK}\left\{-b_K(\delta\varepsilon_v - \delta\varepsilon_{v,p}) + \left[\left(\frac{\delta m}{\rho}\right)_K - \delta\phi_{K,p}\right]\right\}, \quad \ldots\ldots\ldots\ldots\ldots (5)$$

$$\delta\boldsymbol{\kappa} = -\mathbf{H}\cdot\delta\boldsymbol{\xi}, \quad \ldots\ldots\ldots\ldots\ldots\ldots\ldots\ldots (6)$$

where the variation of the elastic fluid content of phase J is

$$\left(\frac{\delta m}{\rho}\right)_{J,e} = \left(\frac{\delta m}{\rho}\right)_J - \delta\phi_{J,p}. \quad \ldots\ldots\ldots\ldots\ldots (7)$$

Here, subscripts e and p denote elastic and plastic, respectively; $\boldsymbol{\varepsilon}$ is the total strain tensor; and $\mathbf{C}_{dr}$ represents the tensor of elastic drained bulk moduli. We define $\boldsymbol{\sigma}'$, the effective stress, in the incremental form as $\delta\boldsymbol{\sigma}' = \mathbf{C}_{dr}{:}\delta\boldsymbol{\varepsilon}_e$, where $\boldsymbol{\sigma}' = \mathbf{0}$ at $\boldsymbol{\varepsilon}_e = \mathbf{0}$. $\boldsymbol{\varepsilon}_e = \boldsymbol{\varepsilon} - \boldsymbol{\varepsilon}_p$ is the elastic strain. The Biot moduli matrix and Biot coefficient are denoted, respectively, by $\mathbf{M} = (M_{JK})$ and $\boldsymbol{b} = (b_J)$. $\boldsymbol{\kappa}$ and $\boldsymbol{\xi}$ are the internal stress-like and strain-like plastic variables, respectively. $\mathbf{H}$ is a hardening modulus matrix. Here, $\mathbf{M}$ and $\mathbf{H}$ are assumed to be positive-definite, which is a sufficient condition for thermodynamic stability

(Coussy 1995). We use the explicit expression of the Biot modulus matrix $\mathbf{M}$ presented in Lewis and Sukirman (1993b) and Lewis and Schrefler (1998). We set $b_J = b\ S_J$ (Lewis and Sukirman 1993b; Coussy et al. 1998; Lewis and Schrefler 1998), where b is the Biot coefficient for single-phase flow (Biot and Willis 1957; Coussy 1995); ε_v indicates the total volumetric strain. The plastic porosity ϕ_p and plastic volumetric strain $\varepsilon_{p,v}$ can be related to each other by assuming that $\delta\phi_p = \beta\delta\varepsilon_{p,v}$. Here, we further assume that $\beta = b$ (Armero 1999), which yields

$$\delta\phi_p = b\delta\varepsilon_{p,v}. \quad \ldots\ldots\ldots\ldots\ldots\ldots\ldots\ldots\ldots\ldots (8)$$

Pressure Definition for Multiphase Problems

There are two widely used definitions of pressure when multiple fluid phases saturate the porous medium: the average pore pressure $\overline{p}$ and the equivalent pore pressure p_E.

Several investigators (Lewis and Sukirman 1993b; Lewis and Schrefler 1998; Rutqvist et al. 2001; Wan 2002; Gai 2004; Yin et al. 2009) write the total stress as

$$\boldsymbol{\sigma} - \boldsymbol{\sigma}_0 = \mathbf{C}_{dr} : (\boldsymbol{\varepsilon} - \boldsymbol{\varepsilon}_p) - b(\overline{p} - \overline{p}_0)\mathbf{1}, \quad \ldots\ldots\ldots\ldots (9)$$

where the subscript 0 denotes the reference state. Eq. 9 is modeled after the assumption that the average pore pressure defined as

$$\overline{p} = S_J p_J, \quad \text{(summation over fluid phases is implied)}, \quad \ldots\ldots\ldots\ldots\ldots\ldots (10)$$

is the appropriate definition when multiple fluid phases occupy the pore space. Then, Eq. 9 leads to

$$\delta\boldsymbol{\sigma} = \mathbf{C}_{dr} : (\delta\boldsymbol{\varepsilon} - \delta\boldsymbol{\varepsilon}_p) - (b_J\delta p_J + \tilde{b}_J\delta S_J)\mathbf{1}, \quad \ldots\ldots\ldots (11)$$

where $\tilde{b}_J = b\ p_J$.

In contrast, Eq. 4 is rooted in the concept of equivalent pore pressure p_E, which is defined as (Coussy 2004)

$$p_E = \overline{p} - U, \quad \ldots\ldots\ldots\ldots\ldots\ldots\ldots\ldots\ldots (12)$$

where U is the surface (interfacial) energy. The interfacial energy U is defined, in incremental form, as

$$\delta U = p_J\delta S_J. \quad \ldots\ldots\ldots\ldots\ldots\ldots\ldots\ldots\ldots (13)$$

Substituting p_E into Eq. 9 instead of $\overline{p}$, we obtain Eq. 4. For an isothermal system with two fluid phases (e.g., oil and water) in the porous medium, the interfacial energy can be determined from the capillary pressure relation with

$$U(S_w) = \int_{S_w}^{1} P_c(S)\mathrm{d}S, \quad \ldots\ldots\ldots\ldots\ldots\ldots (14)$$

where S_w is the water (wetting phase) saturation and P_c is the oil-water capillary pressure relation. The reference condition for U is taken as $U = 0$ when $S_w = 1$.

Compared with Eq. 4, Eq. 11 has an additional term because of capillarity. Coussy (2004) argues that p_E must be used (Eq. 4) instead of $\overline{p}$ (Eq. 11) when capillary forces are significant. Eq. 4 is derived by starting from a continuum description (i.e., macroscopic view) (Coussy 1995, 2004), whereas Eq. 11 is obtained from volume averaging starting from a microscopic description.

Next, we address the question of which pressure definition, $\overline{p}$ or p_E, is appropriate for multiphase flow in porous media. For that purpose, we rely on the fact that, because the coupled physical problem must be dissipative, the constitutive model used should yield a well-posed mathematical statement.

Contractivity of the Mathematical Statement

We analyze the contractivity properties of the mathematical statement of coupled geomechanics and multiphase flow for both $\overline{p}$ and p_E. The analysis is performed using the norm based on the complementary Helmholtz free energy, motivated by Coussy (1995); namely,

$$\|\zeta_m\|^2_{\mathcal{T}_m} = \frac{1}{2}\int_\Omega (\boldsymbol{\sigma}' : \mathbf{C}^{-1}_{dr}\boldsymbol{\sigma}' + \boldsymbol{\kappa}\cdot\mathbf{H}^{-1}\boldsymbol{\kappa} + p_J N_{JK} p_K)d\Omega,$$
$$\mathcal{T}_m := [\zeta_m := (\boldsymbol{\sigma}', \boldsymbol{\kappa}, \boldsymbol{p}) \in \mathbb{S}\times\mathbb{R}^{n_{\text{int}}}\times\mathbb{R}^{n_p} : \sigma'_{ij} \in L^2(\Omega), \kappa_i \in L^2(\Omega), p_J \in L^2(\Omega)], \quad \ldots\ldots\ldots\ldots\ldots (15)$$

where σ'_{ij} and κ_i are the components of $\boldsymbol{\sigma}'$ and $\boldsymbol{\kappa}$, respectively; n_p is the number of fluid phases; and $\boldsymbol{p} = \{p_J\}$. $\mathbf{N} = \{N_{JK}\}$ and $\mathbf{M} = \{M_{JK}\}$, where $\mathbf{M} = \mathbf{N}^{-1}$. $\mathbb{S} = \mathbb{R}^{(n_{\text{dim}}+1)n_{\text{dim}}/2}$ is the vector space of symmetric rank-two tensors (Marsden and Hughes 1983), where n_{dim} is the dimension of the domain Ω. The subscript m denotes multiphase conditions.

We first investigate the contractivity of the coupled problem in Eqs. 4 through 7, which use the equivalent pore pressure, p_E. Let ($\boldsymbol{u}_0$, $\boldsymbol{p}_0$, $\boldsymbol{\xi}_0$) and ($\tilde{\boldsymbol{u}}_0$, $\tilde{\boldsymbol{p}}_0$, $\tilde{\boldsymbol{\xi}}_0$) be two arbitrary initial conditions, and let ($\boldsymbol{u}$, $\boldsymbol{p}$, $\boldsymbol{\xi}$) and ($\tilde{\boldsymbol{u}}$, $\tilde{\boldsymbol{p}}$, $\tilde{\boldsymbol{\xi}}$) be the corresponding solutions, which yield ($\boldsymbol{\sigma}'$, $\boldsymbol{m}$, $\boldsymbol{\kappa}$, $\boldsymbol{\varepsilon}_p$) and ($\tilde{\boldsymbol{\sigma}}'$, $\tilde{\boldsymbol{m}}$, $\tilde{\boldsymbol{\kappa}}$, $\tilde{\boldsymbol{\varepsilon}}_p$), respectively, where $\boldsymbol{m} = \{m_J\}$. The difference between the two solutions is denoted by $\mathrm{d}(\cdot) = (\cdot) - (\tilde{\cdot})$. Let the corresponding solutions from two arbitrary initial conditions be close enough, such that they honor the incremental form of the constitutive relations; namely,

$$\mathrm{d}\boldsymbol{\sigma} = \underbrace{\mathbf{C}_{dr} : (\mathrm{d}\boldsymbol{\varepsilon} - \mathrm{d}\boldsymbol{\varepsilon}_p)}_{d\boldsymbol{\sigma}'} - b_J\mathrm{d}p_J\,\mathbf{1}, \quad \ldots\ldots\ldots\ldots\ldots (16)$$

$$\mathrm{d}p_J = M_{JK}\left\{-b_K(\mathrm{d}\varepsilon_v - \mathrm{d}\varepsilon_{p,v}) + \left[\left(\frac{\mathrm{d}m}{\rho}\right)_K - \mathrm{d}\phi_{p,K}\right]\right\}, \quad \ldots\ldots\ldots\ldots\ldots (17)$$

$$\mathrm{d}\boldsymbol{\kappa} = -\mathbf{H}\cdot\mathrm{d}\boldsymbol{\xi}. \quad \ldots\ldots\ldots\ldots\ldots\ldots\ldots\ldots\ldots (18)$$

Substitution of Eqs. 16 through 18 into Eq. 15 leads to

$$\begin{aligned}\|\mathrm{d}\zeta_m\|^2_{\mathcal{T}_m} &= \frac{1}{2}\int_\Omega (\mathrm{d}\boldsymbol{\sigma}' : \mathbf{C}^{-1}_{dr}\mathrm{d}\boldsymbol{\sigma}' + \mathrm{d}\boldsymbol{\kappa}\cdot\mathbf{H}^{-1}\mathrm{d}\boldsymbol{\kappa} + \mathrm{d}p_J N_{JK}\mathrm{d}p_K)\mathrm{d}\Omega \\ &= \frac{1}{2}\int_\Omega \left\{\mathrm{d}\boldsymbol{\varepsilon}_e : \mathbf{C}_{dr}\mathrm{d}\boldsymbol{\varepsilon}_e + \mathrm{d}\boldsymbol{\xi}\cdot\mathbf{H}\mathrm{d}\boldsymbol{\xi} + \left[\left(\frac{\mathrm{d}m}{\rho}\right)_{J,e} - b_J\mathrm{d}\varepsilon_{e,v}\right]\right. \\ &\qquad \left.\times M_{JK}\left[\left(\frac{\mathrm{d}m}{\rho}\right)_{K,e} - b_K\mathrm{d}\varepsilon_{e,v}\right]\right\}\mathrm{d}\Omega, \\ &= \|\mathrm{d}\chi_m\|^2_{\mathcal{N}_m} \quad \ldots\ldots\ldots\ldots\ldots\ldots\ldots\ldots\ldots\ldots (19)\end{aligned}$$

where we define the norm of $\|\chi_m\|_{\mathcal{N}_m}$ as

$$\|\chi_m\|^2_{\mathcal{N}_m} = \frac{1}{2}\int_\Omega \left\{\boldsymbol{\varepsilon}_e : \mathbf{C}_{dr}\boldsymbol{\varepsilon}_e + \boldsymbol{\xi}\cdot\mathbf{H}\boldsymbol{\xi} + \left[\left(\frac{m}{\rho}\right)_{J,e} - b_J\varepsilon_{e,v}\right]\right. \left.\times M_{JK}\left[\left(\frac{m}{\rho}\right)_{K,e} - b_K\varepsilon_{e,v}\right]\right\}\mathrm{d}\Omega, \quad \ldots\ldots (20)$$

$$\mathcal{N}_m := [\chi := (\boldsymbol{\varepsilon}_e, \boldsymbol{\xi}, \boldsymbol{m}_e) \in \mathbb{S}\times\mathbb{R}^{n_{\text{int}}}\times\mathbb{R}^{n_p} : \varepsilon_{e_{i,j}} \in L^2(\Omega), \xi_i \in L^2(\Omega), m_{J,e} \in L^2(\Omega)], \quad \ldots\ldots\ldots\ldots (21)$$

which originates from the Helmholtz free energy (Coussy 1995).

Because the solutions from two arbitrary initial conditions satisfy the governing equations and the boundary conditions, Eqs. 1 and 3 yield

$$\mathrm{Div}\,\mathrm{d}\boldsymbol{\sigma} = \mathbf{0}, \quad \mathrm{d}\dot{m}_J + \mathrm{Div}\,\mathrm{d}\boldsymbol{w}_J = 0, \quad \ldots\ldots\ldots\ldots\ldots (22)$$

where nonnegative plastic dissipation is assumed for elastoplasticity. Note that homogeneous boundary conditions are obtained. It can be shown that the coupled problem of mechanics and

multiphase flow is contractive relative to the $\|\cdot\|_{\mathcal{N}_m}$ norm. Specifically,

$$\begin{aligned}\frac{\mathrm{d}\|\mathrm{d}\chi_m\|^2_{\mathcal{N}_m}}{\mathrm{d}t} &= \frac{\partial\|\mathrm{d}\chi_m\|^2_{\mathcal{N}_m}}{\partial \mathrm{d}\boldsymbol{\varepsilon}_e} : \mathrm{d}\dot{\boldsymbol{\varepsilon}}_e + \frac{\partial\|\mathrm{d}\chi_m\|^2_{\mathcal{N}_m}}{\partial \mathrm{d}\boldsymbol{\xi}} \cdot \mathrm{d}\dot{\boldsymbol{\xi}} + \frac{\partial\|\mathrm{d}\chi_m\|^2_{\mathcal{N}_m}}{\partial \mathrm{d}m_{J,e}}\mathrm{d}\dot{m}_{J,e} \\ &= \int_\Omega \left\{ \mathrm{d}\boldsymbol{\sigma}' : \mathrm{d}\dot{\boldsymbol{\varepsilon}}_e - \left[\left(\frac{\mathrm{d}m_e}{\rho}\right)_J - b_J \mathrm{d}\varepsilon_{e,v}\right] M_{JK} b_K \mathrm{d}\dot{\varepsilon}_{e,v} \right. \\ &\quad \left. - \mathrm{d}\boldsymbol{\kappa}\cdot\mathrm{d}\dot{\boldsymbol{\xi}} + \left[\left(\frac{\mathrm{d}m_e}{\rho}\right)_J - b_J \mathrm{d}\varepsilon_{e,v}\right] M_{JK}\left(\frac{\mathrm{d}\dot{m}_e}{\rho}\right)_K \right\}\mathrm{d}\Omega \\ &= \int_\Omega \left[\mathrm{d}\boldsymbol{\sigma} : \mathrm{d}\dot{\boldsymbol{\varepsilon}} + \left(\frac{\mathrm{d}p}{\rho}\right)_J \mathrm{d}\dot{m}_J\right]\mathrm{d}\Omega - \underbrace{\int_\Omega (\mathrm{d}\boldsymbol{\sigma}' : \mathrm{d}\dot{\boldsymbol{\varepsilon}}_p + \mathrm{d}\boldsymbol{\kappa}\cdot\mathrm{d}\dot{\boldsymbol{\xi}})\mathrm{d}\Omega}_{D_p^d} \\ &= \int_\Omega [\mathrm{d}\boldsymbol{\sigma}: \mathrm{d}\dot{\boldsymbol{\varepsilon}} - \mathrm{d}p_J \mathrm{Div}(\mathrm{d}\boldsymbol{v}_J)]\,\mathrm{d}\Omega - D_p^d (\text{from Eq. } 22_2) \\ &= -\int_\Omega \mathrm{d}\boldsymbol{v}_J \cdot \mathbf{k}_{JK}^{-1}\,\mathrm{d}\boldsymbol{v}_K\,\mathrm{d}\Omega - D_p^d \le 0, \\ &\quad \left(\because \int_\Omega \mathrm{d}\boldsymbol{\sigma}: \mathrm{d}\dot{\boldsymbol{\varepsilon}} d\Omega = 0 \quad \text{from Eq. } 22_1\right), \qquad \cdots\cdots (23)\end{aligned}$$

where $D_p^d \ge 0$ is satisfied for (nonnegative) plastic dissipation. Note that the divergence theorem and Darcy's law are applied to the last expression, where we write

$$\mathrm{d}\boldsymbol{v}_J = -\mathbf{k}_{JK}\mathbf{Grad}(\mathrm{d}p_K),\ \mathbf{k}_{JK} = \frac{1}{B_J}\frac{\boldsymbol{k}_{p,JK}}{\mu_J},\ v_{J,i} \in H(\mathrm{div}, \Omega), \qquad \cdots\cdots (24)$$

where $v_{J,i}$ is a component of $\boldsymbol{v}_J$.

From Eq. 23, we have

$$\|\chi_m(t) - \tilde{\chi}_m(t)\|_{\mathcal{N}_m} \le \|\chi_{m0} - \tilde{\chi}_{m0}\|_{\mathcal{N}_m} \qquad \cdots\cdots (25)$$

and by use of Eq. 19, we obtain

$$\|\zeta_m(t) - \tilde{\zeta}_m(t)\|_{\mathcal{T}_m} \le \|\zeta_{m0} - \tilde{\zeta}_{m0}\|_{\mathcal{T}_m}, \qquad \cdots\cdots (26)$$

where $(\cdot)_{m0}$ indicates a quantity at the initial (reference) condition. Therefore, the coupled multiphase flow and geomechanics problem expressed in terms of p_E is contractive relative to the norms $\|\cdot\|_{\mathcal{N}_m}$ and $\|\cdot\|_{\mathcal{T}_m}$.

Next, we perform a similar analysis for Eq. 11, where the average pore pressure $\overline{p}$ is used. In this case, we can write

$$\begin{aligned}\frac{\mathrm{d}\|\mathrm{d}\chi_m\|^2_{\mathcal{N}_m}}{\mathrm{d}t} &= \frac{\partial\|\mathrm{d}\chi_m\|^2_{\mathcal{N}_m}}{\partial \mathrm{d}\boldsymbol{\varepsilon}_e} : \mathrm{d}\dot{\boldsymbol{\varepsilon}}_e + \frac{\partial\|\mathrm{d}\chi_m\|^2_{\mathcal{N}_m}}{\partial \mathrm{d}\boldsymbol{\xi}} \cdot \mathrm{d}\dot{\boldsymbol{\xi}} + \frac{\partial\|\mathrm{d}\chi_m\|^2_{\mathcal{N}_m}}{\partial \mathrm{d}m_{J,e}}\mathrm{d}\dot{m}_{J,e} \\ &= \int_\Omega \left\{ \mathrm{d}\boldsymbol{\sigma}' : \mathrm{d}\dot{\boldsymbol{\varepsilon}}_e - \left[\left(\frac{\mathrm{d}m_e}{\rho}\right)_J - b_J \mathrm{d}\varepsilon_{e,v}\right] M_{JK} b_K \mathrm{d}\dot{\varepsilon}_{e,v} \right. \\ &\quad \left. - \mathrm{d}\boldsymbol{\kappa}\cdot\mathrm{d}\dot{\boldsymbol{\xi}} + \left[\left(\frac{\mathrm{d}m_e}{\rho}\right)_J - b_J \mathrm{d}\varepsilon_{e,v}\right] M_{JK}\left(\frac{\mathrm{d}\dot{m}_e}{\rho}\right)_K \right\}\mathrm{d}\Omega \\ &= \int_\Omega \left[\mathrm{d}\boldsymbol{\sigma} : \mathrm{d}\dot{\boldsymbol{\varepsilon}} + \left(\frac{\mathrm{d}p}{\rho}\right)_J \mathrm{d}\dot{m}_J\right]\mathrm{d}\Omega \\ &\quad - \underbrace{\int_\Omega [\mathrm{d}\boldsymbol{\sigma}' : \mathrm{d}\dot{\boldsymbol{\varepsilon}}_p + \mathrm{d}\boldsymbol{\kappa}\cdot\mathrm{d}\dot{\boldsymbol{\xi}}]\mathrm{d}\Omega}_{D_p^d} + \int_\Omega \tilde{b}_J \mathrm{d}S_J \mathbf{1} : \mathrm{d}\dot{\boldsymbol{\varepsilon}}\,\mathrm{d}\Omega \\ &= \underbrace{\int_\Omega \tilde{b}_J \mathrm{d}S_J \mathbf{1} : \mathrm{d}\dot{\boldsymbol{\varepsilon}}\,\mathrm{d}\Omega}_{\text{not always} \le 0} - \int_\Omega \mathrm{d}\boldsymbol{v}_J \cdot \mathbf{k}_{JK}^{-1}\,\mathrm{d}\boldsymbol{v}_K\,\mathrm{d}\Omega - D_p^d \not\le 0, \\ &\qquad \cdots\cdots (27)\end{aligned}$$

where the first term in the last equation may be positive. Thus, Eqs. 9 and 11 do not ensure contractivity relative to the Helmholtz free-energy norm. In other words, because the Helmholtz free energy of the mathematical statement may increase with time, which is unphysical, the well-posedness of the coupled system when using $\overline{p}$ is not guaranteed. Note that in the absence of capillary effects, $\tilde{b}_J \mathrm{d}S_J = 0$, and Eqs. 11 and 4 become identical, for which contractivity is guaranteed.

To illustrate the implications of our findings, we consider one-dimensional (1D) oil-water flow with capillarity and $\dot{\sigma}_v = 0$. From Eqs. 5 and 11, we can write

$$\underbrace{\begin{bmatrix} N_{oo} & N_{ow} \\ N_{wo} & N_{ww}\end{bmatrix}}_{\mathbf{N}}\begin{bmatrix}\dot{p}_o \\ \dot{p}_w\end{bmatrix} + b\begin{bmatrix}S_o \\ S_w\end{bmatrix}\dot{\varepsilon}_v = \begin{bmatrix}-\mathrm{Div}\,\boldsymbol{v}_o + f_o \\ -\mathrm{Div}\,\boldsymbol{v}_w + f_w\end{bmatrix}, \qquad \cdots\cdots (28)$$

$$\dot{\sigma}_v = K_{dr}\dot{\varepsilon}_v - \underbrace{b(S_o\dot{p}_o + S_w\dot{p}_w)}_{b_J\dot{p}_J} - \underbrace{\left[-bP_c\frac{\mathrm{d}S_w}{\mathrm{d}P_c}(\dot{p}_o - \dot{p}_w)\right]}_{\tilde{b}_J\dot{S}_J}, \qquad \cdots\cdots (29)$$

where K_{dr} is the drained bulk modulus and $\mathbf{N}$ is given by (Lewis and Schrefler 1998)

$$\begin{bmatrix} N_{oo} & N_{ow} \\ N_{wo} & N_{ww}\end{bmatrix} = \begin{bmatrix} \phi S_o c_o - \phi\dfrac{\mathrm{d}S_w}{\mathrm{d}P_c} + S_o\dfrac{b-\phi}{K_s}S_o & \phi\dfrac{\mathrm{d}S_w}{\mathrm{d}P_c} + S_o\dfrac{b-\phi}{K_s}S_w \\ \phi\dfrac{\mathrm{d}S_w}{\mathrm{d}P_c} + S_w\dfrac{b-\phi}{K_s}S_o & \phi S_w c_w - \phi\dfrac{\mathrm{d}S_w}{\mathrm{d}P_c} + S_w\dfrac{b-\phi}{K_s}S_w\end{bmatrix}.$$

By substitution of Eq. 29 into Eq. 28 and by use of $\dot{\sigma}_v = 0$, we obtain

$$\underbrace{\left(\underbrace{\begin{bmatrix} N_{oo} & N_{ow} \\ N_{wo} & N_{ww}\end{bmatrix}}_{\mathbf{N}} + \frac{b^2}{K_{dr}}\underbrace{\begin{bmatrix} S_o^2 & S_oS_w \\ S_wS_o & S_w^2\end{bmatrix}}_{\tilde{\mathbf{S}}} - \frac{b^2}{K_{dr}}P_c\frac{\mathrm{d}S_w}{\mathrm{d}P_c}\underbrace{\begin{bmatrix} S_o & -S_o \\ S_w & -S_w\end{bmatrix}}_{\overline{\mathbf{S}}}\right)}_{\mathbf{W}} \times \begin{bmatrix}\dot{p}_o \\ \dot{p}_w\end{bmatrix} = \begin{bmatrix}-\mathrm{Div}\,\boldsymbol{v}_o + f_o \\ -\mathrm{Div}\,\boldsymbol{v}_w + f_w\end{bmatrix}. \qquad \cdots\cdots (30)$$

The positive definiteness of $\mathbf{W}$ (left side of Eq. 30) is not guaranteed because $\overline{\mathbf{S}}$ is indefinite, where the eigenvalues of $\overline{\mathbf{S}}$ are 0, $S_o - S_w$. This is the case even though $\mathbf{N}$ and $\tilde{\mathbf{S}}$ are positive definite and positive semidefinite, respectively. For example, when the fluids and the solid grains are incompressible, and when both $|P_c|$ and $|\mathrm{d}S_w/\mathrm{d}P_c|$ are large enough such that $\tilde{\mathbf{S}}$ can be ignored, the matrix $\mathbf{W}$ can be approximated by

$$\mathbf{W} \approx \frac{1}{P_c'}\begin{pmatrix} -\phi - \dfrac{b^2}{K_{dr}}P_cS_o & -\phi + \dfrac{b^2}{K_{dr}}P_cS_o \\ \phi - \dfrac{b^2}{K_{dr}}P_cS_w & -\phi + \dfrac{b^2}{K_{dr}}P_cS_w\end{pmatrix} \qquad \cdots\cdots (31)$$

where $P_c' = \mathrm{d}P_c/\mathrm{d}S_w$. The eigenvalues in Eq. 31 are

$$\lambda_{1,2} = 0, \qquad -\frac{1}{P_c'}\left[\frac{b^2}{K_{dr}}P_c(1-2S_w) + 2\phi\right]. \qquad \cdots\cdots (32)$$

Because P_c' is negative, we have a large negative eigenvalue when $S_w > 0.5$, $P_c > 0.0$, and b^2P_c/K_{dr} is large. In other words, the average pore pressure $\overline{p}$ may lead to an ill-posed problem for which no (numerical) solution exists.

Numerical Discretization

We use the generalized midpoint rule for time discretization in the mathematical analysis. For space discretization, we use the finite-volume method for flow (Aziz and Settari 1979) and a nodal-based finite-element method for the mechanics (Zienkiewicz et al. 1988; Armero and Simo 1992; Lewis and Sukirman 1993b; Lewis and Schrefler 1998; Armero 1999; Wan et al. 2003; White and Borja 2008). In the finite-volume method, the pressure is at the cell center. In the nodal-based finite-element method, the displacement vector is at the vertices of an element (Hughes 1987). This space discretization strategy has the following characteristics: local mass

conservation at the element level; a continuous displacement field, which allows for tracking the deformation; and convergent approximations with the lowest-order discretization (Jha and Juanes 2007). For a slightly compressible fluid, the stated space discretization provides a stable pressure field (Phillips and Wheeler 2007a, 2007b). It is well known that for incompressible (solid and fluid) systems, nodal-based finite-element methods result in spurious pressure oscillations if equal-order approximations of pressure and displacement (e.g., piecewise continuous interpolation) are used (Vermeer and Verruijt 1981; Murad and Loula 1992, 1994; White and Borja 2008). Stabilization techniques for such spurious pressure oscillations have been studied by several authors (Murad and Loula 1992, 1994; Wan 2002; Truty and Zimmermann 2006; White and Borja 2008).

Sequential-Implicit Schemes

We denote the operator corresponding to Eqs. 1 and 3 by $\mathcal{A}^m$. The superscript m is used to indicate multiple fluid phases. By use of the fully implicit method (FIM), the discrete approximation of $\mathcal{A}^m$ can be written as

$$\begin{bmatrix} \boldsymbol{u}^n \\ \boldsymbol{p}_J^n \end{bmatrix} \xrightarrow{\mathcal{A}^m_{fc}} \begin{bmatrix} \boldsymbol{u}^{n+1} \\ \boldsymbol{p}_J^{n+1} \end{bmatrix}, \quad \text{where} \quad \mathcal{A}^m_{fc}: \begin{cases} \text{Div}\,\boldsymbol{\sigma} + \rho_b \boldsymbol{g} = \boldsymbol{0}, \\ \dot{m}_J + \text{Div}\boldsymbol{w}_J = (\rho f)_J, \end{cases} \quad \cdots\cdots\cdots\cdots\cdots\cdots (33)$$

where we solve the coupled nonlinear equations simultaneously using the Newton-Raphson method. Recall that $\dot{(\cdot)}$ indicates time discretization relative to the motion of the solid skeleton. With FIM, the following linear system

$$\underbrace{\begin{bmatrix} \boldsymbol{K}_m & -\boldsymbol{L}_m^T \\ \boldsymbol{L}_m & \boldsymbol{F}_m \end{bmatrix}}_{\boldsymbol{J}_{fc,m}} \begin{bmatrix} \delta \boldsymbol{u} \\ \delta \boldsymbol{p}_J \end{bmatrix}^{n+1,k} = - \begin{bmatrix} \boldsymbol{R}^u \\ \boldsymbol{R}_J^p \end{bmatrix}^{n+1,k}, \quad \cdots\cdots\cdots (34)$$

must be solved for every Newton iteration. Here, $\boldsymbol{J}_{fc,m}$ is the Jacobian matrix. $\boldsymbol{K}_m$ and $\boldsymbol{L}_m$ are the stiffness and mechanics-flow coupling matrices, respectively. $\boldsymbol{F}_m = \boldsymbol{Q}_m + \Delta t \boldsymbol{T}_m$ is the flow matrix, where $\boldsymbol{Q}_m$ is the compressibility matrix and $\boldsymbol{T}_m$ is the transmissibility matrix. The subscript m, $(\cdot)_m$, denotes multiple fluid phases. Similar to our treatment in Kim et al. (2011a, b, c), sequential-implicit solution strategies are used. Specifically, staggered single-pass schemes are used, in which two implicit problems (one for mechanics and one for flow) are solved in sequence. Here, we focus on the undrained split and the fixed-stress split for multiphase-fluid flow because they show unconditional stability for single-phase flow (Kim et al. 2011a).

Undrained Split. Similar to the treatment for coupled mechanics and single-phase flow, the undrained split for multiphase flow decomposes the original operator $\mathcal{A}^m$ into

$$\begin{bmatrix} \boldsymbol{u}^n \\ \boldsymbol{p}_J^n \end{bmatrix} \xrightarrow{\mathcal{A}^{u,m}_{ud}} \begin{bmatrix} \boldsymbol{u}^{n+1} \\ \boldsymbol{p}_J^* \end{bmatrix} \xrightarrow{\mathcal{A}^{p,m}_{ud}} \begin{bmatrix} \boldsymbol{u}^{n+1} \\ \boldsymbol{p}_J^{n+1} \end{bmatrix},$$
$$\text{where} \quad \begin{cases} \mathcal{A}^{u,m}_{ud}: \text{Div}\,\boldsymbol{\sigma} + \rho_b \boldsymbol{g} = \boldsymbol{0}, \delta m_J = 0, \\ \mathcal{A}^{p,m}_{ud}: \dot{m}_J + \text{Div}\boldsymbol{w}_J = (\rho f)_J, \\ \qquad \dot{\boldsymbol{\varepsilon}}: \text{prescribed}, \end{cases} \quad \cdots\cdots\cdots (35)$$

where the time variation of the mass of the fluids is set to zero (i.e., $\delta m_J = 0$), when solving the mechanics problem. The intermediate pressure p_J^* is calculated locally (and explicitly) after the displacement $\boldsymbol{u}^{n+1}$ is computed. Then, this updated (intermediate) pressure is used in the flow problem. From Eqs. 4 through 8, the constraint $\delta m_J = 0$ yields

$$p_J^* - p_J^n = -M_{JK} b_K (\varepsilon_v^{n+1} - \varepsilon_v^n). \quad \cdots\cdots\cdots\cdots\cdots (36)$$

Eq. 36 involves calculation of $M_{JK} b_K$ and p_J^* locally, but this additional computational cost is negligible compared with solving a global system of flow equations.

Fixed-Stress Split. The fixed-stress approach splits the original operator $\mathcal{A}^m$ as follows:

$$\begin{bmatrix} \boldsymbol{u}^n \\ \boldsymbol{p}_J^n \end{bmatrix} \xrightarrow{\mathcal{A}^{p,m}_{ss}} \begin{bmatrix} \boldsymbol{u}^* \\ \boldsymbol{p}_J^{n+1} \end{bmatrix} \xrightarrow{\mathcal{A}^{u,m}_{ss}} \begin{bmatrix} \boldsymbol{u}^{n+1} \\ \boldsymbol{p}_J^{n+1} \end{bmatrix},$$
$$\text{where} \quad \begin{cases} \mathcal{A}^{p,m}_{ss}: \dot{m}_J + \text{Div}\boldsymbol{w}_J = (\rho f)_J, \delta \dot{\boldsymbol{\sigma}} = \boldsymbol{0}, \\ \mathcal{A}^{u,m}_{ss}: \text{Div}\,\boldsymbol{\sigma} + \rho_b \boldsymbol{g} = \boldsymbol{0}, \boldsymbol{p}_J: \text{prescribed}, \end{cases} \quad \cdots\cdots\cdots\cdots\cdots (37)$$

where the initial condition of the flow problem $\mathcal{A}^p_{ss}$ is determined from the original coupled problem satisfying

$$\text{Div}\dot{\boldsymbol{\sigma}}_{t=0} = \boldsymbol{0}, \quad \text{Div}\,\boldsymbol{\sigma}_{t=0} + \rho_b \boldsymbol{g} = \boldsymbol{0}. \quad \cdots\cdots\cdots\cdots (38)$$

In this scheme, the flow problem is solved first while freezing the time variation of the total stress ($\delta \dot{\sigma} = 0$). As a result, the volumetric total-stress term $(b/K_{dr})\dot{\sigma}_v$ in the accumulation term of Eq. 37 is evaluated explicitly when dealing with the flow problem:

$$\sigma_v^{n+1} - \sigma_v^n = \sigma_v^n - \sigma_v^{n-1}. \quad \cdots\cdots\cdots\cdots\cdots\cdots (39)$$

Note that the use of the elastoplastic moduli implies nonnegative plastic dissipation.

Contractivity of Sequential-Implicit Schemes. In this section, we investigate the contractivity properties of the undrained split and the fixed-stress split. We then investigate their B-stability, which refers to the numerical stability of a specific discrete time-stepping strategy.

Undrained Split. From Eq. 35, we can write

$$\begin{bmatrix} \text{d}\boldsymbol{u}^n \\ \text{d}\boldsymbol{p}_J^n \end{bmatrix} \xrightarrow{\mathcal{A}^{u,m}_{ud}} \begin{bmatrix} \text{d}\boldsymbol{u}^{n+1} \\ \text{d}\boldsymbol{p}_J^* \end{bmatrix} \xrightarrow{\mathcal{A}^{p,m}_{ud}} \begin{bmatrix} \text{d}\boldsymbol{u}^{n+1} \\ \text{d}\boldsymbol{p}_J^{n+1} \end{bmatrix},$$
$$\text{where} \quad \begin{cases} \mathcal{A}^{u,m}_{ud}: \text{Div}\,\text{d}\boldsymbol{\sigma} = \boldsymbol{0}, \delta \text{d}m_J = 0 \\ \mathcal{A}^{p,m}_{ud}: \text{d}\dot{m}_J + \text{Div}(\text{d}\boldsymbol{w}_J) = 0, \\ \quad \text{d}\dot{\boldsymbol{\varepsilon}} = \boldsymbol{0}, \text{d}\dot{\varepsilon}_p = \boldsymbol{0}, \text{d}\dot{\boldsymbol{\xi}} = \boldsymbol{0} \end{cases} \quad \cdots\cdots (40)$$

where nonnegative plastic dissipation is assumed for elastoplasticity, $D_p^d \geq 0$. Note that homogeneous boundary conditions are obtained, just as in Eq. 22. When solving the mechanical problem $\mathcal{A}^{u,m}_{ud}$ of Eq. 40, we obtain

$$\begin{aligned} \frac{\text{d}\|\text{d}\chi_m\|^2_{\mathcal{N}_m}}{\text{d}t} &= \int_\Omega \left[\text{d}\boldsymbol{\sigma} : \text{d}\dot{\boldsymbol{\varepsilon}} + \left(\frac{\text{d}p}{\rho}\right)_J \text{d}\dot{m}_J \right] \text{d}\Omega \\ &\quad - \underbrace{\int_\Omega (\text{d}\boldsymbol{\sigma}' : \text{d}\dot{\boldsymbol{\varepsilon}}_p + \text{d}\boldsymbol{\kappa} \cdot \text{d}\dot{\boldsymbol{\xi}}) \text{d}\Omega}_{D_p^d} = \int_\Omega \text{d}\boldsymbol{\sigma} : \text{d}\dot{\boldsymbol{\varepsilon}} \text{d}\Omega - D_p^d \\ &= -D_p^d \leq 0 \quad (\text{from Eq. } 40_1), \end{aligned} \quad \cdots\cdots\cdots (41)$$

which shows contractivity relative to the norm $\|\cdot\|_{\mathcal{N}_m}$. Then, for the flow problem (i.e., $\mathcal{A}^{p,m}_{ud}$ of Eq. 40), we can write

$$\begin{aligned} \frac{\text{d}\|\text{d}\chi_m\|^2_{\mathcal{N}_m}}{\text{d}t} &= \int_\Omega \left[\text{d}\boldsymbol{\sigma} : \text{d}\dot{\boldsymbol{\varepsilon}} + \left(\frac{\text{d}p}{\rho}\right)_J \text{d}\dot{m}_J \right] \text{d}\Omega - \underbrace{\int_\Omega (\text{d}\boldsymbol{\sigma}' : \text{d}\dot{\boldsymbol{\varepsilon}}_p + \text{d}\boldsymbol{\kappa} \cdot \text{d}\dot{\boldsymbol{\xi}}) \text{d}\Omega}_{D_p^d} \\ &= \int_\Omega - \text{d}p_J \text{Div}(\text{d}\boldsymbol{v}_J) \text{d}\Omega \ (\because \text{d}\dot{\boldsymbol{\varepsilon}} = \boldsymbol{0}, \text{d}\dot{\varepsilon}_p = \boldsymbol{0}, \text{d}\dot{\boldsymbol{\xi}} = \boldsymbol{0}) \\ &= -\int_\Omega \text{d}\boldsymbol{v}_J \cdot \boldsymbol{k}_{JK}^{-1} \text{d}\boldsymbol{v}_K \text{d}\Omega \leq 0, \end{aligned} \quad \cdots\cdots\cdots\cdots (42)$$

which shows contractivity relative to the norm $\|\cdot\|_{\mathcal{N}_m}$. Therefore, the undrained split of coupled mechanics and multiphase flow is contractive relative to the norm $\|\cdot\|_{\mathcal{N}_m}$.

Fixed-Stress Split. From Eq. 37, the fixed-stress split has the form

$$\begin{bmatrix} \mathrm{d}\boldsymbol{u}^n \\ \mathrm{d}\boldsymbol{p}_J^n \end{bmatrix} \xrightarrow{\mathcal{A}_{ss}^{p,m}} \begin{bmatrix} \mathrm{d}\boldsymbol{u}^* \\ \mathrm{d}\boldsymbol{p}_J^{n+1} \end{bmatrix} \xrightarrow{\mathcal{A}_{ss}^{u,m}} \begin{bmatrix} \mathrm{d}\boldsymbol{u}^{n+1} \\ \mathrm{d}\boldsymbol{p}_J^{n+1} \end{bmatrix},$$

$$\text{where} \quad \begin{cases} \mathcal{A}_{ss}^{p,m} : \mathrm{d}\dot{m}_J + \mathrm{Div}\, \mathrm{d}\boldsymbol{w}_J = 0, \delta\mathrm{d}\dot{\boldsymbol{\sigma}} = \boldsymbol{0} \\ \mathcal{A}_{ss}^{u,m} : \mathrm{Div}\ \mathrm{d}\boldsymbol{\sigma} = \boldsymbol{0},\ \mathrm{d}p_J = 0 \\ \quad \Rightarrow \mathrm{Div}\ \mathrm{d}\boldsymbol{\sigma}' = \boldsymbol{0}, \end{cases} \quad \cdots\cdots\cdots\cdots (43)$$

where homogeneous boundary conditions are obtained. Just as for single-phase flow, the condition of nonnegative plastic dissipation is assumed to be valid for multiphase flow.

When the flow problem $\mathcal{A}_{ss}^{p,m}$ is solved, the initial conditions of the stress field (i.e., $\mathrm{Div}\ \mathrm{d}\dot{\boldsymbol{\sigma}}_{t=0} = \boldsymbol{0}$ and $\mathrm{Div}\ \mathrm{d}\boldsymbol{\sigma}_{t=0} = \boldsymbol{0}$) and $\delta\mathrm{d}\dot{\boldsymbol{\sigma}} = \boldsymbol{0}$ yield

$$\mathrm{Div}\, \mathrm{d}\boldsymbol{\sigma} = \boldsymbol{0}, \quad \cdots\cdots\cdots\cdots\cdots\cdots\cdots\cdots (44)$$

from which we obtain

$$\int_\Omega \mathrm{d}\boldsymbol{\sigma} : \mathrm{d}\dot{\boldsymbol{\varepsilon}}\mathrm{d}\Omega = \boldsymbol{0}. \quad \cdots\cdots\cdots\cdots\cdots\cdots\cdots\cdots (45)$$

It follows that for the flow problem solution, we can write

$$\begin{aligned} \frac{\mathrm{d}\|\mathrm{d}\chi_m\|_{\mathcal{N}_m}^2}{\mathrm{d}t} &= \int_\Omega \left[\mathrm{d}\boldsymbol{\sigma} : \mathrm{d}\dot{\boldsymbol{\varepsilon}} + \left(\frac{\mathrm{d}p}{\rho}\right)_J \mathrm{d}\dot{m}_J \right] \mathrm{d}\Omega \\ &\quad - \underbrace{\int_\Omega (\mathrm{d}\boldsymbol{\sigma}' : \mathrm{d}\dot{\boldsymbol{\varepsilon}}_p + \mathrm{d}\boldsymbol{\kappa} \cdot \mathrm{d}\dot{\boldsymbol{\xi}})\mathrm{d}\Omega}_{D_p^{\mathrm{d}}} \\ &= -\int_\Omega (\mathrm{d}\boldsymbol{v}_J \cdot \mathbf{k}_{JK}^{-1}\mu \mathrm{d}\boldsymbol{v}_K)\mathrm{d}\Omega - D_p^d \le 0. \end{aligned} \quad \cdots\cdots\cdots\cdots (46)$$

For solution of the mechanics problem, $\mathcal{A}_{ss}^{u,m}$, we write

$$\begin{aligned} \frac{\mathrm{d}\|\mathrm{d}\chi_m\|_{\mathcal{N}_m}^2}{\mathrm{d}t} &= \int_\Omega \left[\mathrm{d}\boldsymbol{\sigma} : \mathrm{d}\dot{\boldsymbol{\varepsilon}} + \left(\frac{\mathrm{d}p}{\rho}\right)_J \mathrm{d}\dot{m}_J \right] \mathrm{d}\Omega \\ &\quad - \underbrace{\int_\Omega (\mathrm{d}\boldsymbol{\sigma}' : \mathrm{d}\dot{\boldsymbol{\varepsilon}}_p + \mathrm{d}\boldsymbol{\kappa} \cdot \mathrm{d}\dot{\boldsymbol{\xi}})\mathrm{d}\Omega}_{D_p^d} \\ &= \int_\Omega \mathrm{d}\boldsymbol{\sigma}' : \mathrm{d}\dot{\boldsymbol{\varepsilon}}\mathrm{d}\Omega - D_d^{\mathrm{d}} \\ &= D_p^d \le 0,\ \left(\int_\Omega \mathrm{d}\boldsymbol{\sigma}' : \mathrm{d}\dot{\boldsymbol{\varepsilon}}\mathrm{d}\Omega = 0 \text{ from Eq. } 43_2 \right). \end{aligned} \quad \cdots\cdots\cdots\cdots (47)$$

Therefore, the fixed-stress split is contractive relative to $\|\cdot\|_{\mathcal{N}_m}$.

B-Stability of Sequential Implicit Methods. Because the undrained split and the fixed-stress split are contractive, we study their numerical stability with respect to time discretization, which is referred to as B-stability. Here, we measure stability with respect to $\|\cdot\|_{\mathcal{N}_m}$. A time discretization is B-stable if the following condition is satisfied for a contractive problem:

$$\|\mathrm{d}\chi_m^{n+1}\|_{\mathcal{N}_m} \le \|\mathrm{d}\chi_m^n\|_{\mathcal{N}_m}. \quad \cdots\cdots\cdots\cdots\cdots\cdots (48)$$

We use the generalized midpoint rule for time discretization. Therefore, the return-mapping algorithm for elastoplasticity is also on the basis of the generalized midpoint rule. We need the return-mapping algorithm to model nonnegative plastic dissipation for elastoplasticity. In the return mapping, we adopt the associated flow rule (maximum plastic dissipation), which satisfies (Simo 1991; Simo and Govindjee 1991)

$$\ll \boldsymbol{\Sigma}^{tr,n+\alpha} - \boldsymbol{\Sigma}^{n+\alpha}, \boldsymbol{\Pi} - \boldsymbol{\Sigma}^{n+\alpha} \gg \le 0\ {}^\forall\boldsymbol{\Pi} \in \mathcal{E}, \quad \cdots\cdots\cdots\cdots\cdots\cdots (49)$$

where we define the bilinear form $\ll \cdot, \cdot \gg$,

$$\ll \boldsymbol{\Sigma}, \boldsymbol{\Pi} \gg := \int_\Omega (\boldsymbol{\sigma}' : \mathbf{C}_{dr}^{-1}\boldsymbol{\pi}' + \boldsymbol{\kappa} \cdot \mathbf{H}^{-1}\boldsymbol{\eta})\mathrm{d}\Omega, \quad \cdots\cdots (50)$$

and its associated norm $\|\cdot\|_{\mathcal{E}}$,

$$\|\boldsymbol{\Sigma}\|_{\mathcal{E}}^2 := \frac{1}{2} \ll \boldsymbol{\Sigma}, \boldsymbol{\Sigma} \gg, \quad \cdots\cdots\cdots\cdots\cdots (51)$$

where $\boldsymbol{\Sigma} = (\boldsymbol{\sigma}', \boldsymbol{\kappa})$ is a generalized effective stress constrained to lie within the elastic domain $\mathcal{E}$. $\boldsymbol{\Pi} = (\boldsymbol{\pi}', \boldsymbol{\eta})$ is another (arbitrary) generalized effective stress, and $\boldsymbol{\Sigma}^{tr,n+\alpha}$ from the elastic trial step is defined as $(\boldsymbol{\sigma}'^n + \alpha\mathbf{C}_{dr}\Delta\boldsymbol{\varepsilon}^n, \boldsymbol{\kappa}^n)$. Eq. 49 yields

$$\begin{aligned} &\ll \mathrm{d}\boldsymbol{\Sigma}^n - \mathrm{d}\boldsymbol{\Sigma}^{n+\alpha}, \mathrm{d}\boldsymbol{\Sigma}^{n+\alpha} \gg \\ &+ \ll (\alpha\mathbf{C}_{dr}\Delta\mathrm{d}\boldsymbol{\varepsilon}^n, \boldsymbol{0}), (-\mathrm{d}\boldsymbol{\sigma}'^{n+\alpha}, -\mathrm{d}\boldsymbol{\kappa}^{n+\alpha}) \gg \le 0. \end{aligned} \quad \cdots\cdots (52)$$

Undrained Split. In the undrained scheme, one solves a mechanics problem first, followed by the flow problem. We now show B-stability for both steps. The discrete form of the mechanical problem in the undrained split is expressed as

$$\mathrm{Div}\, \mathrm{d}\boldsymbol{\sigma}^{n+\alpha} = \boldsymbol{0},\ \Delta\mathrm{d}m_J = 0, \quad \cdots\cdots\cdots\cdots\cdots (53)$$

which satisfies Eq. 52 as follows. The first term of Eq. 52 can be written as

$$\begin{aligned} &\ll \mathrm{d}\boldsymbol{\Sigma}^n - \mathrm{d}\boldsymbol{\Sigma}^{n+\alpha}, \mathrm{d}\boldsymbol{\Sigma}^{n+\alpha} \gg \\ &= - \ll \alpha\left(\mathrm{d}\boldsymbol{\Sigma}^n - \mathrm{d}\boldsymbol{\Sigma}^{n+1}\right), \mathrm{d}\boldsymbol{\Sigma}^{n+1/2} + \left(\alpha - \frac{1}{2}\right)\left(\mathrm{d}\boldsymbol{\Sigma}^{n+1} - \mathrm{d}\boldsymbol{\Sigma}^n\right) \gg \\ &= \alpha\left(\|\mathrm{d}\boldsymbol{\Sigma}^{n+1}\|_{\mathcal{E}}^2 - \|\mathrm{d}\boldsymbol{\Sigma}^n\|_{\mathcal{E}}^2\right) + \alpha(2\alpha - 1)\|\mathrm{d}\boldsymbol{\Sigma}^{n+1}\|_{\mathcal{E}} - \|\mathrm{d}\boldsymbol{\Sigma}^n\|_{\mathcal{E}}^2. \end{aligned} \quad \cdots\cdots\cdots\cdots (54)$$

Introducing the following identity

$$\begin{aligned} \int_\Omega \mathrm{d}p_J^{n+\alpha} N_{JK}(\mathrm{d}p_K^{n+1} - \mathrm{d}p_K^n)\mathrm{d}\Omega &= (\|\mathrm{d}\boldsymbol{p}^{n+1}\|_{\mathcal{M}}^2 - \|\mathrm{d}\boldsymbol{p}^n\|_{\mathcal{M}}^2) \\ &\quad + (2\alpha - 1)\|\mathrm{d}\boldsymbol{p}^{n+1} - \mathrm{d}\boldsymbol{p}^n\|_{\mathcal{M}}^2, \end{aligned} \quad \cdots\cdots (55)$$

the second term of Eq. 52 becomes

$$\begin{aligned} &\ll (\alpha\mathbf{C}_{dr}\Delta\mathrm{d}\boldsymbol{\varepsilon}^n, \boldsymbol{0}), (-\mathrm{d}\boldsymbol{\sigma}'^{n+\alpha}, -\mathrm{d}\boldsymbol{\kappa}^{n+\alpha}) \gg \\ &= -\int_\Omega \alpha\Delta\mathrm{d}\boldsymbol{\varepsilon}^n : \mathrm{d}\boldsymbol{\sigma}'^{n+\alpha}\mathrm{d}\Omega = -\alpha\int_\Omega \Delta\mathrm{d}\boldsymbol{\varepsilon}^n : (\mathrm{d}\boldsymbol{\sigma}^{n+\alpha} + b_J\mathrm{d}p_J^{n+\alpha}\mathbf{1})\mathrm{d}\Omega \\ &= -\alpha\int_\Omega \Delta\mathrm{d}\boldsymbol{\varepsilon}^n : b_J\mathrm{d}p_J^{n+\alpha}\mathbf{1}\mathrm{d}\Omega \left(\because \int_\Omega \Delta\mathrm{d}\boldsymbol{\varepsilon}^n : \mathrm{d}\boldsymbol{\sigma}^{n+\alpha}\mathrm{d}\Omega = 0 \text{ from Eq. } 53 \right) \\ &= \alpha\int_\Omega \mathrm{d}p_J^{n+\alpha} N_{JK}(\mathrm{d}p_K^{n+1} - \mathrm{d}p_K^n)\mathrm{d}\Omega \\ &[\because b_J\Delta\mathrm{d}\boldsymbol{\varepsilon}^n : \mathbf{1} = -N_{JK}(\mathrm{d}p_K^{n+1} - \mathrm{d}p_K^n) \text{ from } \Delta\mathrm{d}m_J = 0, \text{ Eqs. 8 and 17}] \\ &= \alpha(\|\mathrm{d}\boldsymbol{p}^{n+1}\|_{\mathcal{M}}^2 - \|\mathrm{d}\boldsymbol{p}^n\|_{\mathcal{M}}^2) + \alpha(2\alpha - 1)\|\mathrm{d}\boldsymbol{p}^{n+1} - \mathrm{d}\boldsymbol{p}^n\|_{\mathcal{M}}^2, \end{aligned} \quad \cdots\cdots (56)$$

where $\|\cdot\|_{\mathcal{M}}$ is defined as

$$\|\boldsymbol{p}\|_{\mathcal{M}}^2 = \frac{1}{2}\int_\Omega p_J N_{JK} p_K \mathrm{d}\Omega. \quad \cdots\cdots\cdots\cdots\cdots (57)$$

Using Eqs. 52, 54, and 56 yields

$$\begin{aligned} &\alpha\left[\|\mathrm{d}\boldsymbol{\Sigma}^{n+1}\|_{\mathcal{E}}^2 - \|\mathrm{d}\boldsymbol{\Sigma}^n\|_{\mathcal{E}}^2 + \left(\|\mathrm{d}\boldsymbol{p}^{n+1}\|_{\mathcal{M}}^2 - \|\mathrm{d}\boldsymbol{p}^n\|_{\mathcal{M}}^2\right)\right] \\ &+ \alpha(2\alpha - 1)\left(\|\mathrm{d}\boldsymbol{\Sigma}^{n+1} - \mathrm{d}\boldsymbol{\Sigma}^n\|_{\mathcal{E}}^2 + \|\mathrm{d}\boldsymbol{p}^{n+1} - \mathrm{d}\boldsymbol{p}^n\|_{\mathcal{M}}^2\right) \le 0. \end{aligned} \quad \cdots\cdots\cdots\cdots (58)$$

From Eq. 58, the mechanics-problem solution can be expressed as

$$\begin{aligned}&\|\mathrm{d}\chi_m^{n+1}\|_{\mathcal{N}_m}^2 - \|\mathrm{d}\chi_m^{n}\|_{\mathcal{N}_m}^2\\&= \|\mathrm{d}\boldsymbol{\Sigma}^{n+1}\|_{\mathcal{E}}^2 + \|\mathrm{d}\boldsymbol{p}^{n+1}\|_{\mathcal{M}}^2 - \|\mathrm{d}\boldsymbol{\Sigma}^{n}\|_{\mathcal{E}}^2 - \|\mathrm{d}\boldsymbol{p}^{n}\|_{\mathcal{M}}^2\\&\le -(2\alpha-1)\left(\|\mathrm{d}\boldsymbol{\Sigma}^{n+1} - \mathrm{d}\boldsymbol{\Sigma}^{n}\|_{\mathcal{E}}^2 + \|\mathrm{d}\boldsymbol{p}^{n+1} - \mathrm{d}\boldsymbol{p}^{n}\|_{\mathcal{M}}^2\right).\end{aligned} \quad \cdots\cdots\cdots\cdots\cdots\cdots (59)$$

Eq. 59 indicates that the undrained split has B-stability when $0.5 \le \alpha \le 1$ for the mechanical problem.

The discrete form of the flow problem $\mathcal{A}_{ud}^{p,m}$ (Eq. 40) can be written as

$$N_{JK}\frac{\mathrm{d}p_K^{n+1} - \mathrm{d}p_K^{n}}{\Delta t} + b_J\frac{\mathrm{d}\varepsilon_v^{n+1} - \mathrm{d}\varepsilon_v^{n}}{\Delta t} + \mathrm{Div}(\mathrm{d}\boldsymbol{v}_J^{n+\alpha}) = 0, \quad \cdots\cdots\cdots\cdots\cdots\cdots (60)$$

$$\Delta\mathrm{d}\boldsymbol{\varepsilon} = \boldsymbol{0},\ \Delta\mathrm{d}\boldsymbol{\varepsilon}_p = \boldsymbol{0},\ \Delta\mathrm{d}\boldsymbol{\xi} = \boldsymbol{0}. \quad \cdots\cdots\cdots\cdots (61)$$

By use of Darcy's law, Eqs. 60 and 61 lead to

$$\begin{aligned}\int_\Omega \mathrm{d}p_J^{n+\alpha}N_{JK}\left(\frac{\mathrm{d}p_K^{n+1} - \mathrm{d}p_K^{n}}{\Delta t}\right)\mathrm{d}\Omega &= \int_\Omega \mathbf{Grad}\,\mathrm{d}p_J^{n+\alpha}\cdot\mathrm{d}\boldsymbol{v}_J^{n+\alpha}\mathrm{d}\Omega\\&= -\int_\Omega \mathrm{d}\boldsymbol{v}_J^{n+\alpha}\cdot\mathbf{k}_{JK}^{-1}\mathrm{d}\boldsymbol{v}_K^{n+\alpha}\mathrm{d}\Omega\ (\because \mathbf{Grad}\,\mathrm{d}p_J^{n+\alpha} = -\mathbf{k}_{JK}^{-1}\mathrm{d}\boldsymbol{v}_K^{n+\alpha}).\end{aligned} \quad \cdots\cdots\cdots\cdots\cdots\cdots (62)$$

In turn, Eq. 61 implies

$$\|\mathrm{d}\boldsymbol{\Sigma}^{n+1}\|_{\mathcal{E}}^2 = \|\mathrm{d}\boldsymbol{\Sigma}^{n}\|_{\mathcal{E}}^2. \quad \cdots\cdots\cdots\cdots (63)$$

From Eqs. 55, 62, and 63, we have

$$\begin{aligned}&\|\mathrm{d}\chi_m^{n+1}\|_{\mathcal{N}_m}^2 - \|\mathrm{d}\chi_m^{n}\|_{\mathcal{N}_m}^2 = \|\mathrm{d}\boldsymbol{p}^{n+1}\|_{\mathcal{M}}^2 - \|\mathrm{d}\boldsymbol{p}^{n}\|_{\mathcal{M}}^2\\&= -(2\alpha-1)\|\mathrm{d}\boldsymbol{p}^{n+1} - \mathrm{d}\boldsymbol{p}^{n}\|_{\mathcal{M}}^2 - \Delta t\int_\Omega \mathrm{d}\boldsymbol{v}_J^{n+a}\cdot\mathbf{k}_{JK}^{-1}\mathrm{d}\boldsymbol{v}_K^{n+a}\mathrm{d}\Omega,\end{aligned} \quad \cdots\cdots\cdots\cdots\cdots\cdots (64)$$

which shows that B-stability is obtained for $0.5 \le \alpha \le 1$. From the mechanics problem (Eq. 59) and the flow problem (Eq. 64), the undrained sequential-implicit scheme is B-stable for $0.5 \le \alpha \le 1$.

Fixed-Stress Split. We show B-stability of the fixed-stress split in which the flow problem is solved first, followed by the mechanics problem. The discrete form of the flow problem is written as

$$N_{JK}\frac{\mathrm{d}p_K^{n+1} - \mathrm{d}p_K^{n}}{\Delta t} + b_J\frac{\mathrm{d}\varepsilon_v^{n+1} - \mathrm{d}\varepsilon_v^{n}}{\Delta t} + \mathrm{Div}(\mathrm{d}\boldsymbol{v}_J^{n+\alpha}) = 0, \quad \cdots\cdots\cdots\cdots\cdots\cdots (65)$$

$$\mathrm{d}\boldsymbol{\sigma}^{n+1} - \mathrm{d}\boldsymbol{\sigma}^{n} = \mathrm{d}\boldsymbol{\sigma}^{n} - \mathrm{d}\boldsymbol{\sigma}^{n-1}, \quad \cdots\cdots\cdots\cdots (66)$$

where the initial conditions for the stress field satisfy

$$\mathrm{Div}(\mathrm{d}\boldsymbol{\sigma}^{1} - \mathrm{d}\boldsymbol{\sigma}^{0}) = \boldsymbol{0},\ \mathrm{Div}\,\mathrm{d}\boldsymbol{\sigma}^{0} = \boldsymbol{0}. \quad \cdots\cdots\cdots\cdots (67)$$

Then, Eqs. 66 and 67 lead to

$$\mathrm{Div}\,\mathrm{d}\boldsymbol{\sigma}^{n+\alpha} = \boldsymbol{0}, \quad \cdots\cdots\cdots\cdots\cdots\cdots (68)$$

which, when we solve the flow problem, yields

$$\int_\Omega \mathrm{d}\boldsymbol{\sigma}^{n+\alpha} :\ \Delta\mathrm{d}\boldsymbol{\varepsilon}^{n}\mathrm{d}\Omega = 0. \quad \cdots\cdots\cdots\cdots (69)$$

Note that we consider maximum plastic dissipation in the flow step because we use the elastoplastic moduli, which are obtained from the return-mapping algorithm. Because maximum plastic dissipation is assumed for the flow problem, Eq. 52 is satisfied. Also, note that Eq. 54 is an identity.

Now, we consider the second term of Eq. 52, which is calculated as follows:

$$\begin{aligned}&\ll (\alpha\mathbf{C}_{dr}\Delta\mathrm{d}\boldsymbol{\varepsilon}^{n}, \boldsymbol{0}), (-\mathrm{d}\boldsymbol{\sigma}'^{n+\alpha}, -\mathrm{d}\boldsymbol{\kappa}^{n+\alpha}) \gg\\&= -\int \alpha\Delta\mathrm{d}\boldsymbol{\varepsilon}^{n} : \mathrm{d}\boldsymbol{\sigma}'^{n+\alpha}\mathrm{d}\Omega\\&= -\alpha\int \Delta\mathrm{d}\boldsymbol{\varepsilon}^{n} : (\mathrm{d}\boldsymbol{\sigma}^{n+\alpha} + b_J\mathrm{d}p_J^{n+\alpha}\mathbf{1})\mathrm{d}\Omega\\&= -\alpha\int \Delta\mathrm{d}\varepsilon_v^{n}b_J\mathrm{d}p_J^{n+\alpha}\mathrm{d}\Omega\ (\text{from Eq. 69}).\end{aligned} \quad \cdots\cdots\cdots (70)$$

From Eqs. 54 and 70, Eq. 52 can be written as

$$\begin{aligned}&(\|\mathrm{d}\boldsymbol{\Sigma}^{n+1}\|_{\mathcal{E}}^2 - \|\mathrm{d}\boldsymbol{\Sigma}^{n}\|_{\mathcal{E}}^2) + (2\alpha-1)\|\mathrm{d}\boldsymbol{\Sigma}^{n+1} - \mathrm{d}\boldsymbol{\Sigma}^{n}\|_{\mathcal{E}}^2\\&- \int \Delta\mathrm{d}\varepsilon_v^{n}b_J\mathrm{d}p_J^{n+\alpha}\mathrm{d}\Omega \le 0.\end{aligned} \quad \cdots\cdots\cdots\cdots\cdots (71)$$

The flow-equation operator, $\mathcal{A}_{ss}^{p,m}$ (Eq. 65), has the following property

$$\begin{aligned}\int\Bigg(&\mathrm{d}p_J^{n+\alpha}N_{JK}\frac{\mathrm{d}p_K^{n+1} - \mathrm{d}p_K^{n}}{\Delta t} + b_J\frac{\mathrm{d}\varepsilon_v^{n+1} - \mathrm{d}\varepsilon_v^{n}}{\Delta t}\\&+ \mathrm{Div}(\mathrm{d}\boldsymbol{v}_J^{n+\alpha})\Bigg)\mathrm{d}\Omega = 0.\end{aligned} \quad \cdots\cdots\cdots\cdots\cdots (72)$$

Using the identity of Eq. 55 and Darcy's law, Eq. 72 becomes

$$\begin{aligned}&\|\mathrm{d}\boldsymbol{p}^{n+1}\|_{\mathcal{M}}^2 - \|\mathrm{d}\boldsymbol{p}^{n}\|_{\mathcal{M}}^2 = -(2\alpha-1)\|\mathrm{d}\boldsymbol{p}^{n+1} - \mathrm{d}\boldsymbol{p}^{n}\|_{\mathcal{M}}^2\\&- \int \mathrm{d}p_J^{n+\alpha}b_J\Delta\mathrm{d}\varepsilon_v^{n}\mathrm{d}\Omega - \Delta t\int \mathrm{d}\boldsymbol{v}_J^{n+\alpha}\cdot\mathbf{k}_{JK}^{-1}\mathrm{d}\boldsymbol{v}_K^{n+\alpha}\mathrm{d}\Omega.\end{aligned} \quad \cdots\cdots\cdots\cdots\cdots\cdots (73)$$

Thus, for the flow-problem treatment in the fixed-stress scheme, the evolution of the norm $\|\cdot\|_{\mathcal{N}_m}$ can be analyzed by adding Eqs. 71 and 73. We then have

$$\begin{aligned}&\|\mathrm{d}\chi_m^{n+1}\|_{\mathcal{N}_m}^2 - \|\mathrm{d}\chi_m^{n}\|_{\mathcal{N}_m}^2\\&= \|\mathrm{d}\boldsymbol{\Sigma}^{n+1}\|_{\mathcal{E}}^2 + \|\mathrm{d}\boldsymbol{p}^{n+1}\|_{\mathcal{M}}^2 - \|\mathrm{d}\boldsymbol{\Sigma}^{n}\|_{\mathcal{E}}^2 - \|\mathrm{d}\boldsymbol{p}^{n}\|_{\mathcal{M}}^2\\&\le -(2\alpha-1)\left(\|\mathrm{d}\boldsymbol{\Sigma}^{n+1} - \mathrm{d}\boldsymbol{\Sigma}^{n}\|_{\mathcal{E}}^2 + \|\mathrm{d}\boldsymbol{p}^{n+1} - \mathrm{d}\boldsymbol{p}^{n}\|_{\mathcal{M}}^2\right)\\&-\Delta t\int \mathrm{d}\boldsymbol{v}_J^{n+\alpha}\cdot\mathbf{k}_{JK}^{-1}\mathrm{d}\boldsymbol{v}_K^{n+\alpha}\mathrm{d}\Omega.\end{aligned} \quad \cdots\cdots\cdots\cdots\cdots (74)$$

This expression shows that B-stability is obtained for the flow problem, if $0.5 \le \alpha \le 1$.

Now, for the mechanics problem, from Eq. 43, we have

$$\mathrm{Div}\,\mathrm{d}\boldsymbol{\sigma}'^{n+\alpha} = \boldsymbol{0},\ \mathrm{d}\boldsymbol{p}^{n+\alpha} = \boldsymbol{0}, \quad \cdots\cdots\cdots\cdots\cdots (75)$$

to which maximum plastic dissipation, Eq. 52, is applied. The second term of Eq. 52 is expressed as

$$\begin{aligned}&\ll (\alpha\mathbf{C}_{dr}\Delta\mathrm{d}\boldsymbol{\varepsilon}^{n}, \boldsymbol{0}), (-\mathrm{d}\boldsymbol{\sigma}'^{n+\alpha}, -\mathrm{d}\boldsymbol{\kappa}^{n+\alpha}) \gg\\&= -\int \alpha\Delta\mathrm{d}\boldsymbol{\varepsilon}^{n} : \mathrm{d}\boldsymbol{\sigma}'^{n+\alpha}\mathrm{d}\Omega = 0.\end{aligned} \quad \cdots\cdots\cdots\cdots\cdots (76)$$

Using Eqs. 54 and 76, Eq. 52 becomes

$$(\|\mathrm{d}\boldsymbol{\Sigma}^{n+1}\|_{\mathcal{E}}^2 - \|\mathrm{d}\boldsymbol{\Sigma}^{n}\|_{\mathcal{E}}^2) + (2\alpha-1)\|\mathrm{d}\boldsymbol{\Sigma}^{n+1} - \mathrm{d}\boldsymbol{\Sigma}^{n}\|_{\mathcal{E}}^2 \le 0. \quad \cdots\cdots\cdots\cdots\cdots (77)$$

Because $\mathrm{d}p_J^{n+\alpha} = 0$, Eq. 55 can be written as

$$\|\mathrm{d}\boldsymbol{p}^{n+1}\|_{\mathcal{M}}^2 - \|\mathrm{d}\boldsymbol{p}^{n}\|_{\mathcal{M}}^2 = -(2\alpha-1)\|\mathrm{d}\boldsymbol{p}^{n+1} - \mathrm{d}\boldsymbol{p}^{n}\|_{\mathcal{M}}^2. \quad \cdots\cdots\cdots\cdots\cdots (78)$$

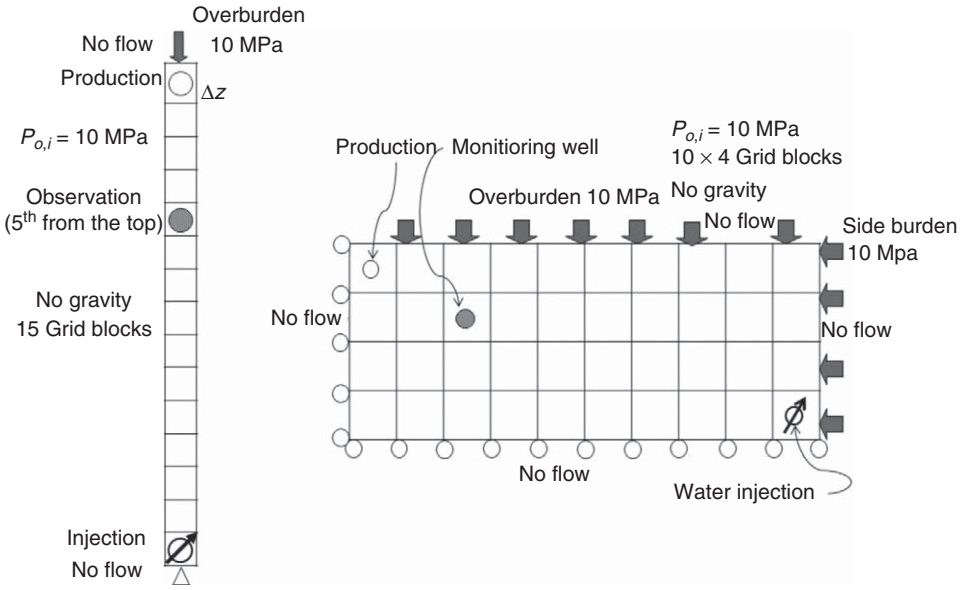

Fig. 1—Water injection and oil production. Left: coupled multiphase flow and geomechanics in a 1D poroelastic medium. Right: coupled multiphase flow and geomechanics in a 2D poroelastic medium with overburden and side burden.

Then, Eqs. 77 and 78 yield

$$\begin{aligned}&\|\mathrm{d}\chi_m^{n+1}\|_{\mathcal{N}_m}^2 - \|\mathrm{d}\chi_m^{n}\|_{\mathcal{N}_m}^2\\&= \|\mathrm{d}\boldsymbol{\Sigma}^{n+1}\|_{\mathcal{E}}^2 - \|\mathrm{d}\boldsymbol{\Sigma}^{n}\|_{\mathcal{E}}^2 + \|\mathrm{d}\boldsymbol{p}^{n+1}\|_{\mathcal{M}}^2 - \|\mathrm{d}\boldsymbol{p}^{n}\|_{\mathcal{M}}^2\\&\le -(2\alpha-1)\left(\|\mathrm{d}\boldsymbol{\Sigma}^{n+1} - \mathrm{d}\boldsymbol{\Sigma}^{n}\|_{\mathcal{E}}^2 + \|\mathrm{d}\boldsymbol{p}^{n+1} - \mathrm{d}\boldsymbol{p}^{n}\|_{\mathcal{M}}^2\right),\end{aligned} \quad \ldots\ldots\ldots\ldots\ldots\ldots (79)$$

which shows that B-stability is obtained if $0.5 \le \alpha \le 1$ for the mechanics problem, $\mathcal{A}_{ss}^{u,m}$. Therefore, from Eqs. 74 and 79, the fixed-stress split is B-stable if $0.5 \le \alpha \le 1$.

Numerical Results

We test the applicability of the equivalent pore pressure (p_E) and average pore pressure ($\overline{p}$) definitions for immiscible two-phase-flow (e.g., oil and water) problems with mechanical deformation. **Fig. 1** shows the setup of the two test cases. The backward-Euler method is used for time discretization. We take oil pressure and water saturation as primary variables in our numerical discretization, and understand that oil and water represent the nonwetting and wetting fluid phases, respectively.

Case 1: Water Injection and Oil Production in a 1D Poroelastic Medium. The schematic of this 1D problem is shown in the left plot of Fig. 1. The water injection rate $Q_{w,\mathrm{inj}} = 500\ \mathrm{kg{\cdot}d^{-1}}$ is the same as the total liquid production rate $Q_{o,\mathrm{prod}} = 500\ \mathrm{kg{\cdot}d^{-1}}$. The length of the homogeneous domain is $L_z = 15$ m. The overburden stress is $\overline{\sigma} = 10.0$ MPa. A no-displacement boundary condition is maintained at the bottom of the domain. The bulk density of the porous medium is $\rho_b = 2400\ \mathrm{kg{\cdot}m^{-1}}$. The formation is initially fully saturated with oil, and the initial oil pressure is $P_{o,i} = 10.0$ MPa. The fluid densities and viscosities are $\rho_{o,0} = \rho_{w,0} = 1000\ \mathrm{kg{\cdot}m^{-1}}$ and $\mu_o = \mu_w = 1.0$ cp, respectively. With the same density for oil and water, we effectively neglect the effect of gravity. The medium permeability is $k_p = 50$ md, the porosity is $\phi_0 = 0.1$, the constrained modulus is $K_{dr} = 20.0$ MPa, and the Biot coefficient is $b = 1.0$. Low values of the bulk modulus—even much lower than the value of K_{dr} used here—can be found in sandy clay, soft clay, or weakly consolidated porous media under low confining stress (Maswoswe 1985; Josa et al. 1987; Josa 1988; Terzaghi et al. 1996; Alonso et al. 1990). The oil and water compressibilities are $c_o = 4.0 \times 10^{-9}\ \mathrm{Pa^{-1}}$ and $c_w = 4.0 \times 10^{-10}\ \mathrm{Pa^{-1}}$, respectively. No-flow boundary conditions are applied at the top and bottom. We discretize the domain with grid spacing $\Delta z = 1.0$ m (i.e., 15 grid blocks) and track the pressure at the fifth gridblock from the top. We use a timestep size of 0.025 days.

We use power-law (Corey-type) relative-permeabilities:

$$k_{r,J} = (S_J - S_{r,J})^{l_J}, \quad \ldots\ldots\ldots\ldots\ldots\ldots\ldots (80)$$

where $S_{r,J}$ is the residual saturation of phase J and l_J is the exponent that characterizes the relative permeability curve of phase J **(Fig. 2).** To test the numerical stability and accuracy in the presence of capillarity, we use the capillary pressure model used in Coussy (2004), which is expressed as

$$P_c - P_e = \Pi_c (1/S_w^e - 1)^{l_p},\ S^e = \frac{S_w - S_{r,w}}{1 - S_{r,o} - S_{r,w}}, \quad \ldots. (81)$$

where P_c is the capillary pressure between oil and water, P_e is the capillary entry pressure, and Π_c is the capillary modulus. The exponent l_p characterizes the shape of the capillary pressure curve, which becomes flat as l_p decreases (Fig. 2). We use different values of Π_c to test the formulations on the basis of the average and equivalent pore pressures. In the numerical examples, the residual oil and water saturations are assumed to be zero.

We define the following three nondimensional quantities:

$$\tau = \frac{b_J M_{JK} b_K}{K_{dr}},\ \eta = \frac{\Delta P_o}{\Pi_c},\ \chi = \frac{b^2 \Pi_c}{K_{dr}}, \quad \ldots\ldots\ldots\ldots (82)$$

where ΔP_o is the characteristic oil pressure difference between the injection and production wells. Parameter τ is the coupling strength of flow and geomechanics (Kim et al. 2011a), and η is a capillary number that represents the ratio of large-scale viscous forces compared with the capillary forces. For low values of η, flow is dominated by capillary forces. We introduce the dimensionless quantity χ, motivated by Eq. 32, to investigate the stability and accuracy of deformable systems for various levels of capillarity. From Eq. 82, high values of χ imply high coupling strength and strong capillarity. For the parameter values used here, $\tau = 1.25 \times 10^2$ for oil and $\tau = 1.25 \times 10^3$ for water. Parameters η and χ take different values depending on the value of Π_c.

Here we are interested in testing the stability properties of the two definitions of effective stress (on the basis of p_E and $\overline{p}$), for different levels of capillarity. To that end, it is useful to compare the results against a reference solution. This is possible in the present case, similar to the classical Terzaghi problem in a 1D poroelastic medium with a single-phase fluid and homogeneous

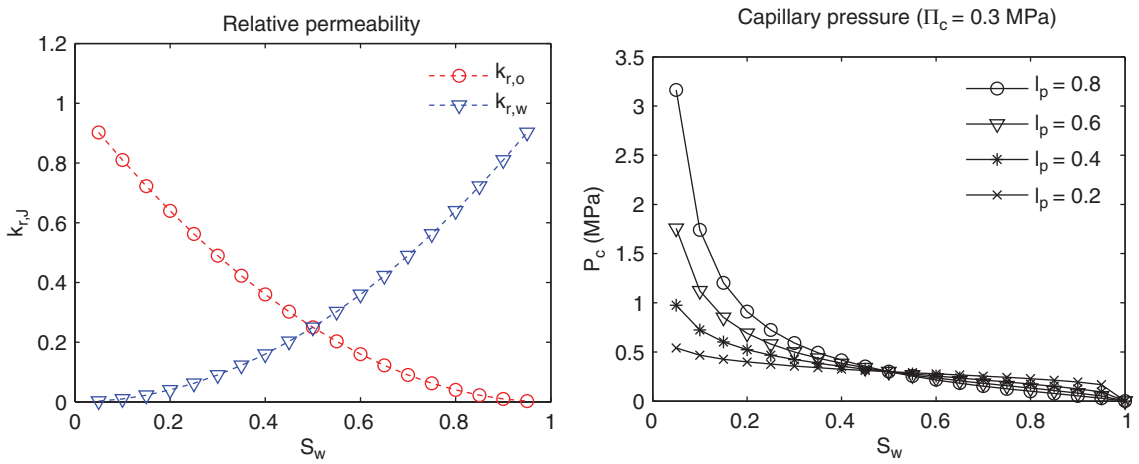

Fig. 2—Left: The shape of the relative permeability curves (Eq. 80) when $l_J = 2.0$ for both oil and water. Right: The shape of the capillary pressure curve used in Coussy (2004) (Eq. 81). As the exponent l_p decreases, the capillary pressure curve becomes flat.

boundary conditions. For the classical Terzaghi problem, the flow and mechanics problems decouple. This is true also for multiphase flow when the capillary pressure is constant over the entire range of saturations (i.e., $\delta P_c \approx 0$). We can reproduce these conditions by use of the capillary pressure functional form in Eq. 81 with $l_p = 0$. In this case, Π_c plays the role of the capillary entry pressure (we set P_e to zero). Thus, although the capillary pressure curves are flat, capillarity effects are important if the value of Π_c is high. Finally, we use quadratic relative permeabilities (i.e., $l_o = l_w = 2.0$ in Eq. 80).

To avoid any ambiguity with regard to the influence of the coupling scheme, we use a fully implicit, monolithic solution strategy for both definitions of the pore pressure under multiphase-flow conditions. In **Fig. 3** we show the evolution of the oil

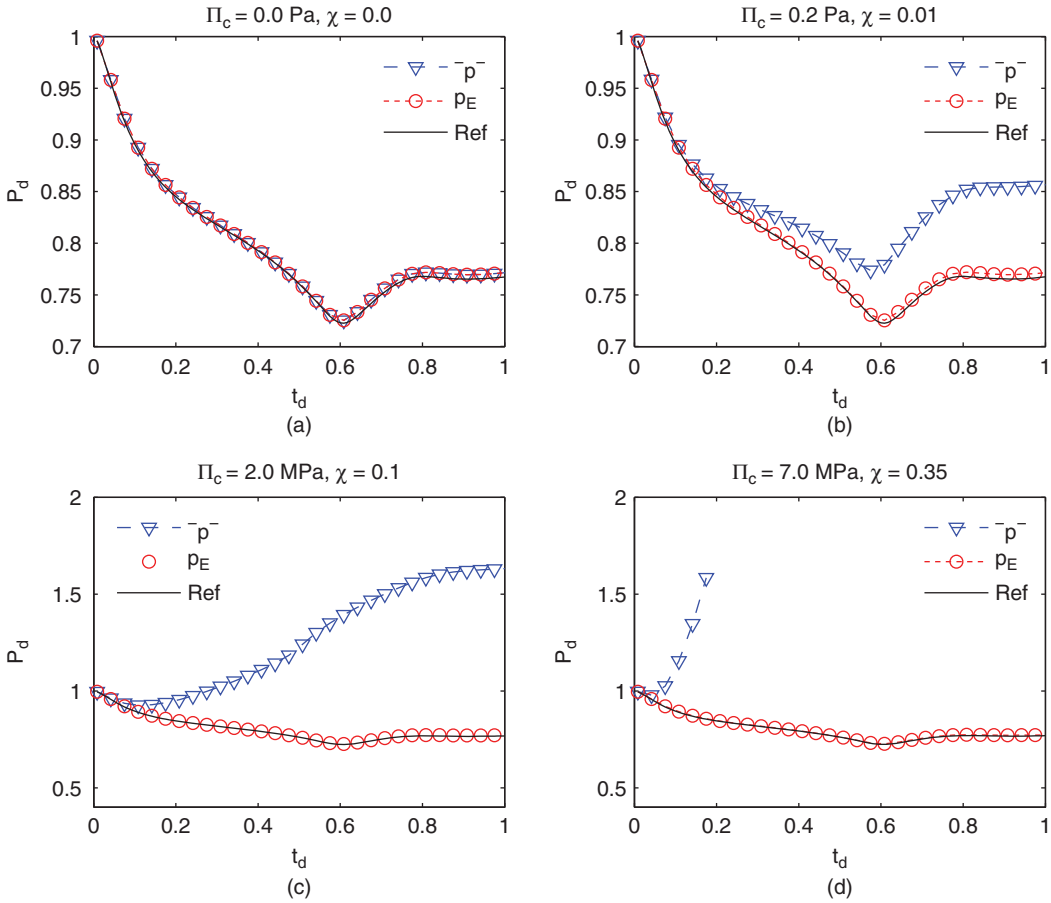

Fig. 3—Evolution of the oil pressure at the observation well in the 1D example. We compare the numerical solutions based on the average pore pressure ($\bar{p}$, blue triangles) and the equivalent pore-pressure (p_E, red circles) with the results from the reference solution (black solid line), for different values of the capillary modulus Π_c. We plot the dimensionless pressure $P_d = \dfrac{p_o - p_L}{p_{o,i} - p_L}$ as a function of dimensionless time $t_d = (Q_{w,inj}/M_t)t$, where p_L is a lower limit of the pressure during simulation (here, we take $p_L = 9.5$ MPa) and M_t is the total initial liquid mass in place. (a) $\Pi_c = 0.0$ Pa; (b) $\Pi_c = 0.2$ MPa; (c) $\Pi_c = 2.0$ MPa. (d) $\Pi_c = 7.0$ MPa. The results from the $\bar{p}$ formulation are increasingly inaccurate for higher values of Π_c, and eventually become unstable for a sufficiently high value of Π_c. The results from the p_E formulation, in contrast, are stable and accurate for all values of Π_c.

TABLE 1—VALUES OF η AND χ FOR DIFFERENT VALUES OF Π_c IN CASE 1

Π_c	0.0 Pa	0.2 MPa	2.0 MPa	7.0 MPa
η	∞	8.6	0.86	0.25
χ	0	0.01	0.1	0.35

pressure at the observation well on the basis of the average pore-pressure $\overline{p}$ and the equivalent pore-pressure p_E. Without capillarity ($\Pi_c = 0$), there is no difference between the two formulations, and they both match the reference solution (Fig. 3a). However, as capillarity increases ($\Pi_c = 0.2$ MPa and 2.0 MPa, corresponding to $\chi = 0.01$ and 0.1, respectively), the results based on $\overline{p}$, although stable, show large errors, whereas those based on p_E agree exactly with the reference solutions (Figs. 3b and 3c). If the strength of the capillary forces is large ($\Pi_c = 7.0$ MPa, corresponding to $\chi = 0.35$), the solution based on the $\overline{p}$ formulation becomes unstable, and blows up at finite time (Fig. 3d).

This numerical behavior can be explained by the a priori estimates of the nonzero eigenvalue of the Jacobian matrix (Eq. 32). For the cases $\Pi_c = 0$, 0.2, and 2 MPa, the eigenvalues are positive for the entire range of saturations (Figs. 4a, 4b, 4c, respectively). In contrast, for the case $\Pi_c = 7$ MPa, the nonzero eigenvalue takes negative values in the range of high water saturations (Fig. 4d), suggesting that one should expect an unstable solution with the $\overline{p}$ pore-pressure formulation, even with a fully implicit monolithic solution strategy.

In **Table 1** we report the values of η and χ for different values of Π_c. As η decreases, χ also increases, and the errors of the $\overline{p}$-based approach become larger. For very large values of χ, numerical instabilities are observed, and this is consistent with the a priori estimates of negative eigenvalues in Eq. 32. Numerical instabilities associated with the use of the average pore pressure $\overline{p}$ cannot be removed by reducing the timestep size or by refining the grid size. In **Fig. 5** we show how the oil pressure, computed with both $\overline{p}$ and p_E, changes when the timestep and grid size are refined by a factor of 10. These results illustrate that refinement does not lead to an improvement in the accuracy of the $\overline{p}$ formulation.

The a priori estimates in Eq. 32 also indicate that numerical stability and accuracy of the $\overline{p}$ formulation also depend on porosity: lower porosity values lead to less-accurate solutions. This dependence is confirmed by numerical results. We performed simulations for two cases: (i) initial porosity $\phi_0 = 1.0 \times 10^{-2}$ and injection/production rates $Q_{w,\mathrm{inj}} = Q_{o,\mathrm{prod}} = 500$ kg·d^{-1}, (ii) smaller initial porosity $\phi_0 = 1.0 \times 10^{-3}$ and reduced injection/production rates $Q_{w,\mathrm{inj}} = Q_{o,\mathrm{prod}} = 50$ kg·d^{-1}. The two cases yield the same dimensionless timestep size because the initial liquid mass in place is reduced by the same factor as the porosity. In **Figs. 6a and 6b,** we show the evolution of the oil pressure at the observation well for both cases. We find that the $\overline{p}$ formulation becomes unstable for the low-porosity case, whereas the p_E formulation is accurate in both cases. The instability of the $\overline{p}$ formulation can again be explained from the behavior of the nonzero eigenvalue, which becomes negative for water saturations $S_w > 0.6$. This finding points to the instability of the $\overline{p}$ formulation for low-porosity formations, even for moderate values of the capillary modulus.

Case 2: Water Injection and Oil Production in a 2D Poroelastic Medium. We sketch the 2D waterflooding example in a 2D homogeneous domain in the right plot of Fig. 1. The dimensions of the domain are 100×20 m, which we discretize into 10×4 gridblocks under the plane-strain mechanical condition. The injection and production wells are at the bottom-right

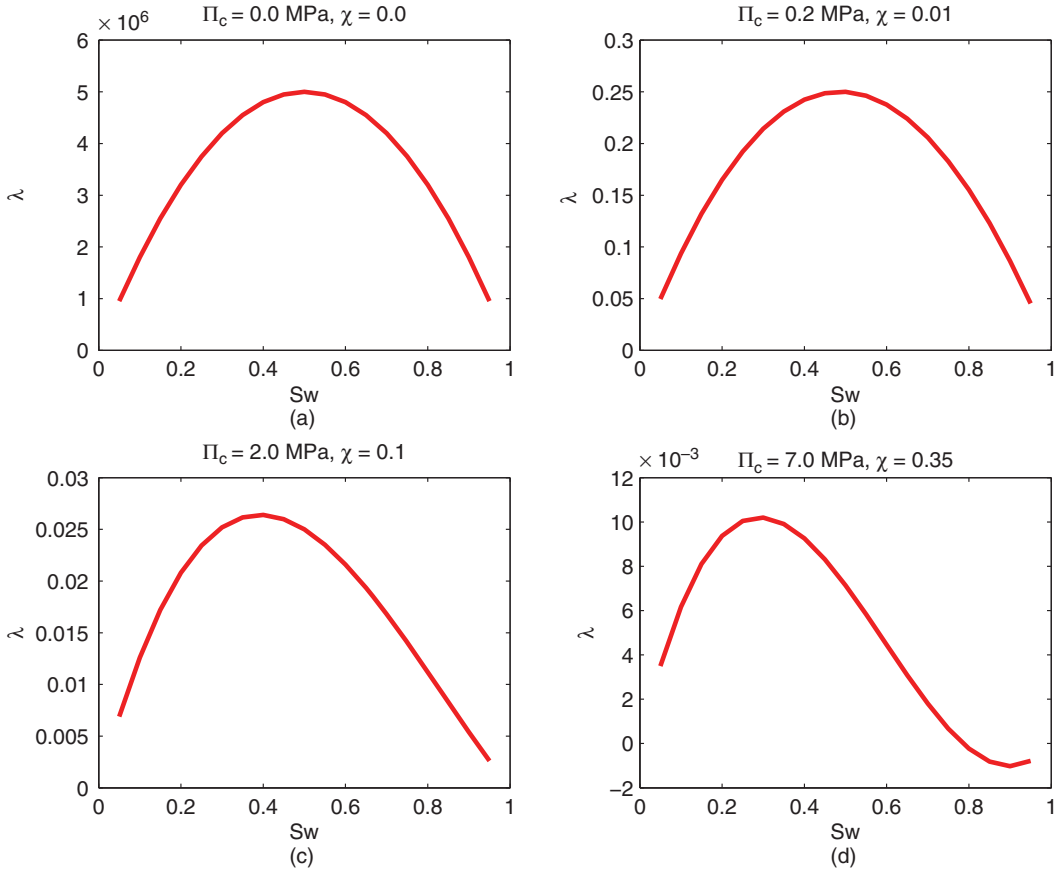

Fig. 4—Nonzero eigenvalue of the Jacobian matrix (Eq. 32) in the 1D example when using the average pore pressure formulation ($\overline{p}$), as a function of water saturation, and for different values of the capillary modulus Π_c. (a) $\Pi_c \approx 0.0$ Pa; (b) $\Pi_c = 0.2$ MPa; (c) $\Pi_c = 2.0$ MPa; (d) $\Pi_c = 7.0$ MPa. For $\Pi_c = 7.0$ MPa, the eigenvalue becomes negative in the range of high water saturations, suggesting that one should expect an unstable solution.

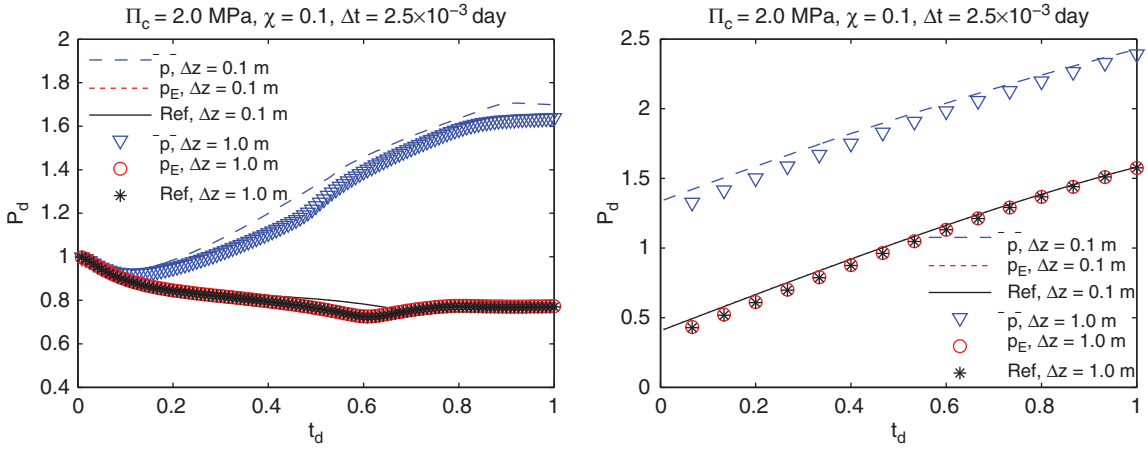

Fig. 5—Comparison of oil pressure based on the $\bar{p}$ and p_E formulations when the timestep size and/or the grid size are refined. Left: Evolution of dimensionless oil pressure P_d at the monitoring point. Right: Dimensionless oil pressure profile as a function of dimensionless depth $z_d = z/L_z$, at dimensionless time $t_d = 1.0$. Grid size and timestep refinements do not improve the accuracy of the $\bar{p}$-formulation results.

and top-left corners, respectively. The water injection rate is the same as the total-liquid production rate, $Q_{w,\mathrm{inj}} = Q_{\mathrm{prod}} = 5000$ kg·d^{-1}. We record pressures and saturations at a "monitoring well" at gridblock (2,3). The boundary conditions are as follows: an overburden of $\bar{\sigma} = 10.0$ MPa is applied on the top boundary; no horizontal displacement at the left boundary; a side burden of $\bar{\sigma}_h = 10.0$ MPa is applied at the right boundary; and no vertical displacement at the bottom boundary. No-flow boundary conditions are applied at all sides.

The bulk density of the porous medium is $\rho_b = 2400$ kg·m^{-1}. The medium is initially fully saturated with oil, and the initial oil pressure is $p_{o,i} = 10.0$ MPa. The density and viscosity of water are $\rho_{w,0} = 1000$ kg·m^{-3} and $\mu_w = 1.0$ cp, respectively. The density and viscosity of oil are $\rho_{o,0} = 1000$ kg·m^{-3} and $\mu_o = 1.0$ cp, respectively. The permeability is $k_p = 500$ md, and the porosity is $\phi_0 = 0.1$. Gravity effects are negligible because the two fluids have the same density. The Young modulus is $E = 24.0$ MPa, and the Poisson ratio is $\nu = 0.3$. The Biot coefficient is $b = 1.0$. From

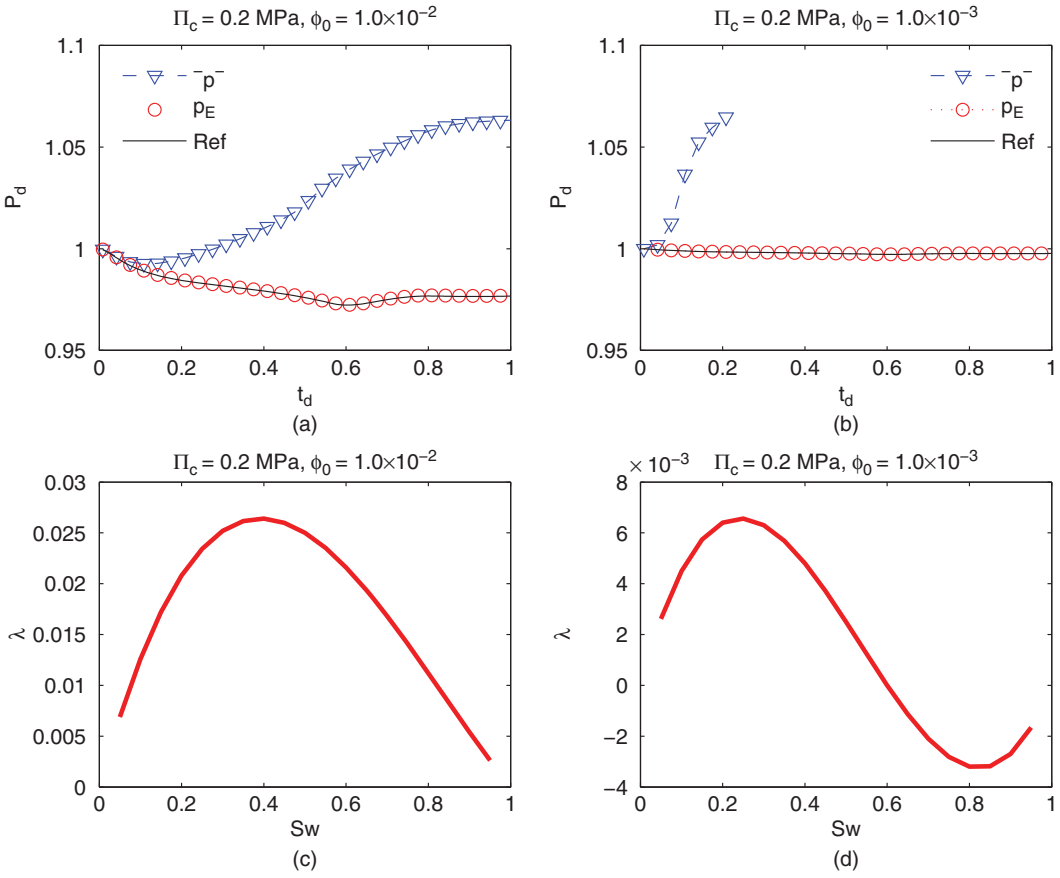

Fig. 6—Comparison of the oil pressure at the observation well for the 1D example when the initial porosity is reduced by a factor of 10 and 100. (a) $\phi_0 = 1.0 \times 10^{-2}$ and $Q_{w,\mathrm{inj}} = Q_{o,\mathrm{prod}} = 500$ kg·d^{-1}; (b) $\phi_0 = 1.0 \times 10^{-3}$ and $Q_{w,\mathrm{inj}} = Q_{o,\mathrm{prod}} = 50$ kg·d^{-1}; (c) eigenvalues for $\phi_0 = 1.0 \times 10^{-2}$; (d) eigenvalues for $\phi_0 = 1.0 \times 10^{-3}$.

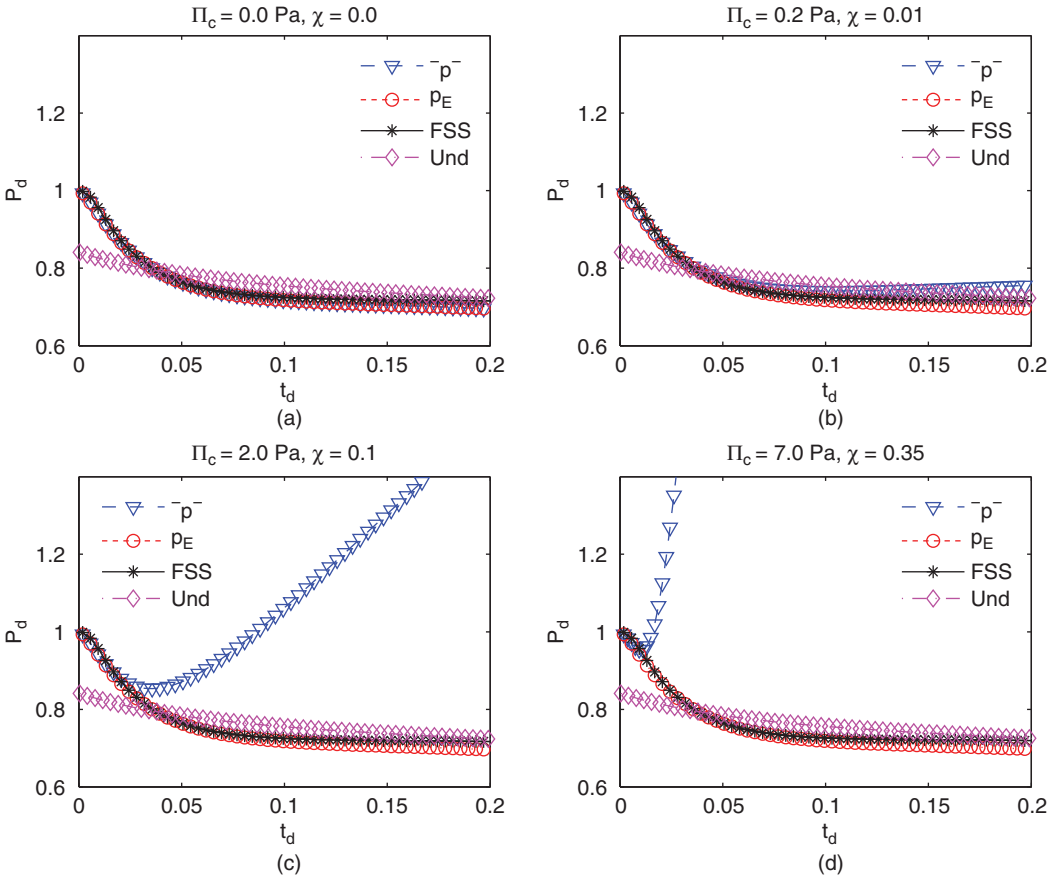

Fig. 7—Evolution of the dimensionless oil pressure at the observation well in the 2D example. We compare the numerical solutions with a fully implicit monolithic strategy on the basis of the average pore pressure ($\overline{p}$, blue triangles) and the equivalent pore pressure (p_E, red circles), for different values of the capillary modulus Π_c. (a) $\Pi_c = 0$ Pa; (b) $\Pi_c = 0.2$ MPa; (c) $\Pi_c = 2.0$ MPa; (d) $\Pi_c = 7.0$ MPa. We also plot the numerical solutions for the p_E formulation with two different sequential solution schemes: the fixed-stress split (black asterisks) and the undrained split (Und, magenta diamonds).

the given Young modulus and Poisson ratio, the drained bulk modulus is $K_{dr} = 20.0$ MPa, the same value of the previous 1D test case. The compressibilities of oil and water are $c_o = 4.0 \times 10^{-9}$ Pa^{-1} and $c_w = 4.0 \times 10^{-10}$ Pa^{-1}, respectively. These fluid compressibility values yield $\tau = 1.25 \times 10^2$ and $\tau = 1.25 \times 10^3$ for single-phase oil and single-phase water, respectively. We use quadratic relative permeabilities and the residual oil and water saturations are assumed to be zero, as in the 1D case. In our simulations, we use a timestep size $\Delta t = 0.075$ days.

Comparison Between the Average- and Equivalent-Pore-Pressure Formulations. We use the same capillary pressure curve used in the 1D problem, taking an exponent $l_p = 0$ and different values of the capillary modulus Π_c to test the performance of the two formulations of the multiphase effective stress, on the basis of the average pore pressure $\overline{p}$ and the equivalent pore pressure p_E. Here, we use a fully implicit, simultaneous solution method to solve the coupled flow-mechanics problem at each timestep.

In **Fig. 7** we show that the average-pore-pressure formulation leads to numerical instabilities when the capillary pressure effects are important—that is, when parameter χ is large (in our 2D example, this happens for values of $\chi > 0.35$; **Table 2**). Even when the solutions based on the average pore pressure are stable, the errors become large for strong capillarity (i.e., low η and high χ). In contrast, the results from the equivalent-pore-pressure p_E show that the numerical solutions are stable regardless of the magnitude of capillarity (Fig. 7).

TABLE 2—VALUES OF η AND χ FOR DIFFERENT VALUES OF Π_c IN CASE 2

Π_c	0.0 Pa	0.2 MPa	2.0 MPa	7.0 MPa
η	∞	3.84	0.384	0.110
χ	0	0.01	0.1	0.35

Comparison Between the Undrained Split and the Fixed-Stress Split. After demonstrating that the equivalent pore pressure p_E (unlike the average pore pressure $\overline{p}$) leads to a stable formulation for a fully implicit monolithic scheme, we now compare the fixed-stress and undrained sequential-implicit solution schemes of the p_E formulation.

In Fig. 7 we show that both the undrained and the fixed-stress operator splits are stable, even in the case of high capillary pressure (Fig. 7d)—in agreement with our nonlinear stability analysis of multiphase flow and geomechanics by use of the energy method. However, it is apparent that the undrained split suffers from loss of accuracy regardless of the magnitude of the capillary pressure, even though the timestep size is five times smaller than that used in the fully implicit monolithic method. The origin of this loss of accuracy of the undrained method is its intrinsic dependence on the coupling strength (Kim et al. 2011b). As the timestep size is reduced, the undrained split yields more accurate solutions, although it still shows noticeable errors even though the timestep size is reduced by one order of magnitude **(Fig. 8).** In contrast, the fixed-stress split yields accurate solutions even when the timestep size is the same as that used in the fully implicit method (Fig. 8), because the accuracy of the fixed-stress split does not depend on the coupling strength (Kim et al. 2011c).

To further confirm this behavior, we run a test case with disparate values of the oil and water compressibilities, $c_o = 4.0 \times 10^{-7}$ Pa^{-1} and $c_w = 4.0 \times 10^{-12}$ Pa^{-1}, which results in a wide range of the coupling strength during the simulation (from

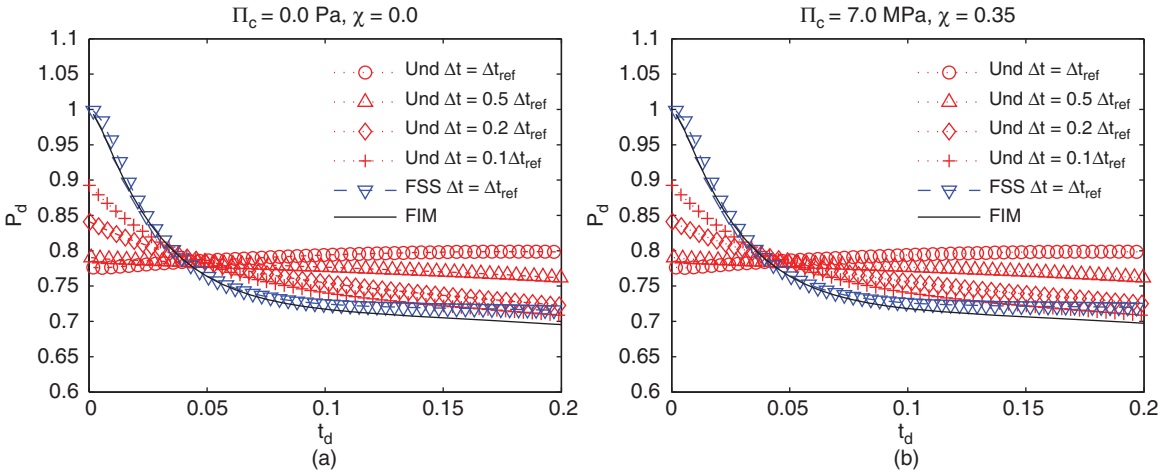

Fig. 8—Convergence of the undrained split as a function of timestep size. Δt_{ref} is the timestep size used in the fixed-stress and fully implicit method in Fig. 7. (a) $\Pi_c = 0.0$ Pa; (b) $\Pi_c = 7.0$ MPa. As the timestep size becomes smaller, the accuracy of the undrained method is enhanced, but it is still lower than that of the fixed-stress method.

1.25 to 1.25×10^5). This allows us to investigate the numerical stability and convergence of the two sequential methods when the fluid system becomes nearly incompressible as water injection progresses.

As the water saturation increases, and as a consequence of the increase in coupling strength τ, the undrained split deviates from the reference fully implicit solution **(Fig. 9).** Although it provides stable solutions in this test case, for high coupling strength, the undrained split yields very stiff subproblems for both flow and mechanics, resulting in ill-conditioned matrices for both subproblems (Kim et al. 2011b). In contrast, the fixed-stress split yields stable and accurate solutions, even for very high coupling strength, matching the fully implicit solution at all times (Fig. 9). Moreover, the fixed-stress split yields less stiff subproblems, which result in better condition numbers, even in the regime of high capillarity.

Accuracy of the Average-Pore-Pressure Approach. Our analysis leading to the expression of the eigenvalue λ in Eq. 32 indicates that the stability and accuracy of the $\bar{p}$-based formulation are compromised as the value of parameter $\chi = b^2\Pi_c/K_{dr}$ increases. This implies that small capillary pressures can cause large errors when the rock stiffness is small and, conversely, that large capillary pressures may induce small errors when the rock stiffness is large. This behavior is shown in **Fig. 10,** where we plot solutions obtained with the $\bar{p}$ and p_E formulations for high capillarity ($\Pi_c = 7.0$ MPa) and two different values of K_{dr}. As the drained bulk modulus increases from $K_{dr} = 2$ GPa to $K_{dr} = 200$ GPa (χ decreases; **Table 3**), the difference in the solutions obtained with the two different pore-pressure definitions decreases. Even though capillarity is strong, a stiffer bulk modulus results in lower values of τ and χ. As χ decreases, the average-pore-pressure formulation becomes numerically stable (Fig. 10a) and the errors decrease (Fig. 10b).

Nonlinear Capillary Pressure Curve. After investigating the effect of high capillarity (high values of Π_c or, equivalently, χ) with a flat capillary pressure curve, we now show an example with a nonlinear P_c curve. We take $\Pi_c = 0.2$ MPa, $P_e = 10$ kPa, and an exponent $l_p = 0.4$. This leads to a highly nonlinear P_c curve, especially in the range of low water saturations. We take $S_{r,o} = S_{r,w} = 0$.

In **Fig. 11** we compare the solutions from the $\bar{p}$ and p_E formulations, both computed with a fully implicit monolithic scheme. There is a noticeable difference between $\bar{p}$ and p_E in the evolution of the oil pressure at the monitoring well (Fig. 11a) and the spatial distribution of oil pressure at the top layer (Fig. 11b), indicating that the $\bar{p}$ formulation is inaccurate even at moderate levels of capillarity.

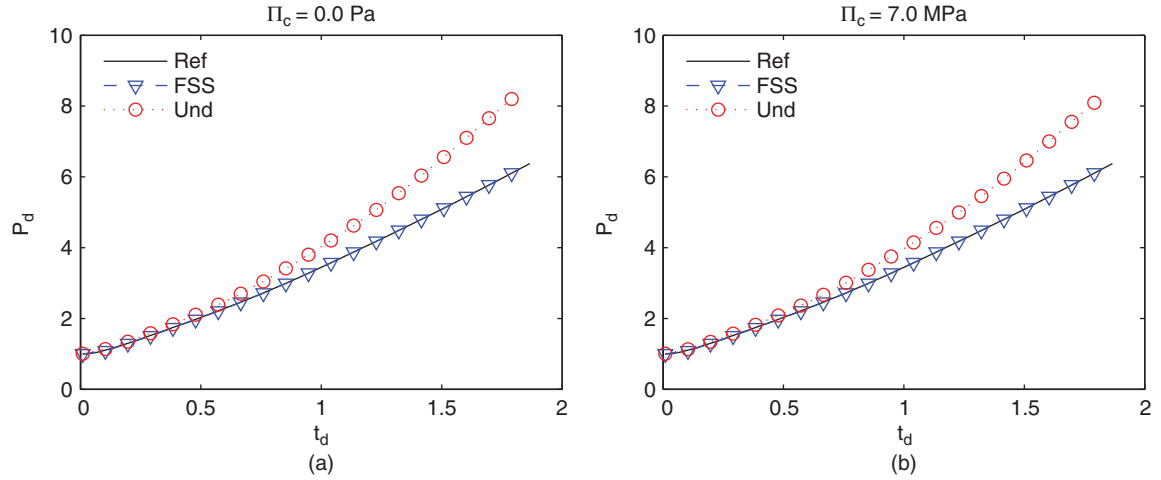

Fig. 9—Evolution of oil pressures by the undrained split and the fixed-stress split based on the p_E formulation for $c_o = 4.0 \times 10^{-7}$ Pa^{-1} and $c_w = 4.0 \times 10^{-12}$ Pa^{-1}. The undrained split exhibits large errors caused by high coupling strength, regardless of capillarity, as water saturates the reservoir. The reference solution is obtained by the fully implicit monolithic method using the equivalent pore pressure.

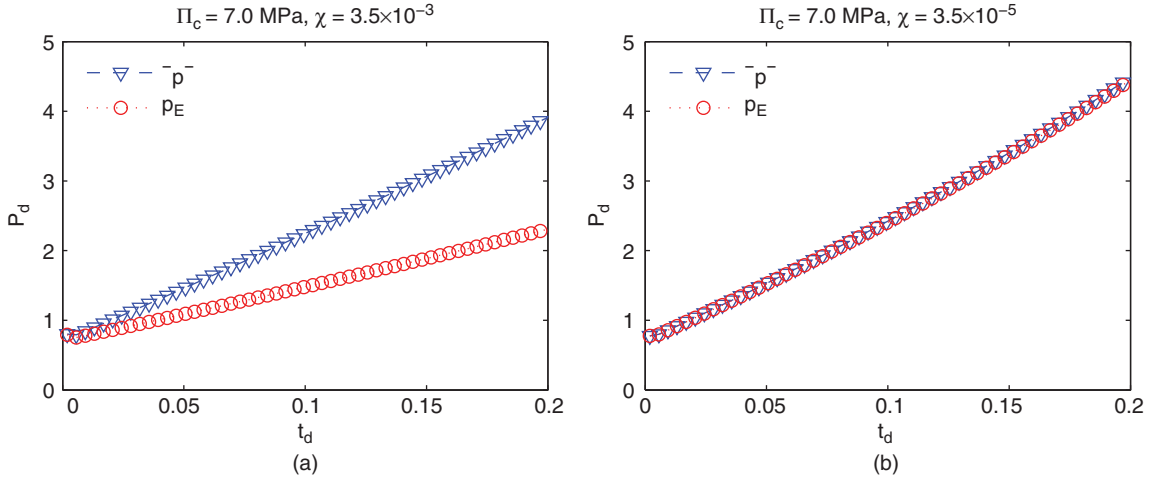

Fig. 10—Evolution of oil pressures on the basis of the $\bar{p}$ and p_E formulations for $\Pi_c = 7.0$ MPa. (a) $K_{dr} = 2$ GPa; (b) $K_{dr} = 200$ GPa. As Π_c/K_{dr} decreases, the accuracy of $\bar{p}$ increases, and the results agree with those of the p_E formulation.

TABLE 3—VARIATION OF τ AND χ FOR DIFFERENT VALUES OF K_{dr}

K_{dr}	20.0 MPa	2.0 GPa	200.0 GPa
τ	$125-1.25\times10^{3}$	1.25–12.5	0.0125–0.125
χ	0.35	3.5×10^{-3}	3.5×10^{-5}

Conclusions

In this work, we have analyzed strategies for the solution of coupled flow and geomechanics in the presence of multiple fluid phases and, therefore, capillarity effects. First, we addressed the question of what is the appropriate definition of pore pressure in the multiphase extension of effective stress.

We investigated two definition; the (saturation-weighted) average pore pressure $\bar{p}$ and the equivalent pore-pressure of Coussy (2004), p_E, from the perspective of nonlinear stability, as well as accuracy and convergence of coupled mechanics and multiphase flow.

Our a priori estimates using the energy method show that p_E is the proper definition of the multiphase pore pressure because it renders a formulation that is demonstrably dissipative, a key property that the $\bar{p}$ formulation does not enjoy. We conduct numerical simulations with a fully implicit monolithic scheme that show, in agreement with our nonlinear stability analysis, that the p_E formulation leads to unconditionally stable and accurate solutions, whereas $\bar{p}$ leads to numerically unstable solutions for strong capillarity. Our simulations also show that even when the $\bar{p}$-based solutions are stable, they deviate significantly from the physically correct reference solution.

After demonstrating that p_E is the appropriate definition of pore pressure in the conservation equations and constitutive relations when multiple fluids occupy the pore space, we then performed stability and convergence analyses of sequential-implicit coupling strategies. We show that the multiphase extensions of both the undrained split and the fixed-stress split (Kim et al. 2011b, 2011c) are unconditionally stable (B-stable). Our analysis and numerical simulations also show that the fixed-stress split is superior to the undrained split in terms of convergence behavior. Even with strong capillarity in near-incompressible systems, the fixed-stress split matches the fully implicit monolithic solution.

Acknowledgments

The first author thanks Eric Sonnenthal and George Moridis from the Lawrence Berkeley National Laboratory for detailed discussions on applications related to geothermal and hydrate reservoirs. This work was supported by the Stanford University Petroleum Research Institute for Reservoir Simulation (SUPRI-B); the American Recovery and Reinvestment Act through the Assistant Secretary for Energy Efficiency and Renewable Energy, Office of Technology Development, Geothermal Technologies Program, of the US Department of Energy under Contract No. DE-AC02-

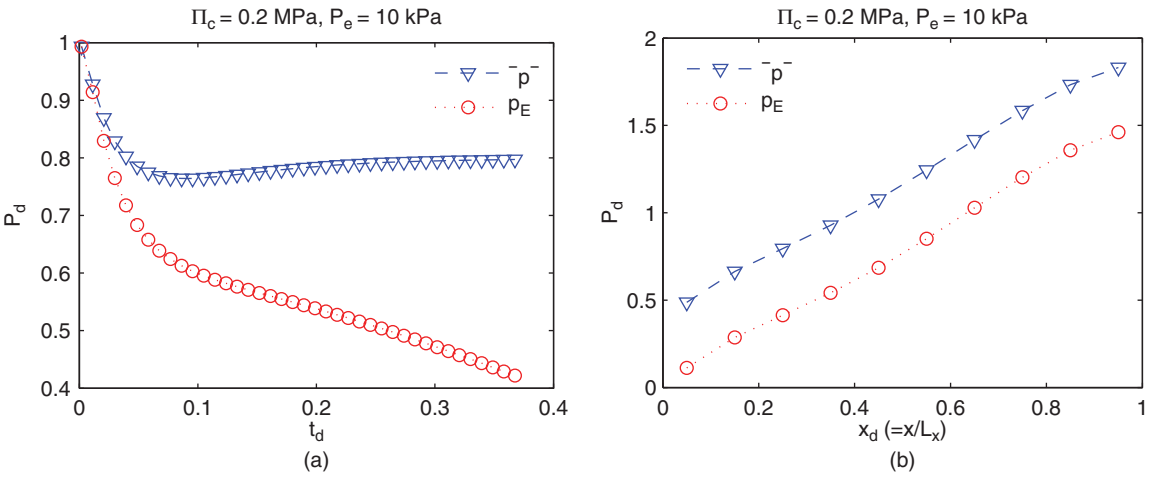

Fig. 11—Comparison of the $\bar{p}$ and p_E formulations for a case with nonlinear capillary pressure. (a) Evolution of dimensionless oil pressure at the monitoring well. (b) Oil pressure distribution at the top layer, where the horizontal distance x is normalized by the horizontal length of the domain L_x. Results are for capillary modulus $\Pi_c = 0.2$ MPa and exponent $l_p = 0.4$ in Eq. 81.

05CH11231; and the Massachusetts Institute of Technology Arco Chair in Energy Studies.

References

Alonso, E.E., Gens, A., and Josa, A. 1990. A Constitutive Model for Partially Saturated Soils. *Geotechnique* **40** (3): 405–430. http://dx.doi.org/10.1680/geot.1990.40.3.405.

Armero, F. 1999. Formulation and Finite Element Implementation of a Multiplicative Model of Coupled Poro-Plasticity at Finite Strains Under Fully Saturated Conditions. *Comput. Methods Appl. Mech. Eng.* **171** (3–4): 205–241. http://dx.doi.org/10.1016/S0045-7825(98)00211-4.

Armero, F. and Simo, J.C. 1992. A New Unconditionally Stable Fractional Step Method for Non-Linear Coupled Thermomechanical Problems. *Int. J. Numer. Meth. Eng.* **35** (4): 737–766. http://dx.doi.org/10.1002/nme.1620350408.

Armero, F. and Simo, J.C. 1993. A Priori Stability Estimates and Unconditionally Stable Product Formula Algorithms for Nonlinear Coupled Thermoplasticity. *Int. J. Plasticity* **9** (6): 749–782. http://dx.doi.org/10.1016/0749-6419(93)90036-P.

Aziz, K. and Settari, A. 1979. *Petroleum Reservoir Simulation*. London, UK: Elsevier.

Bagheri, M. and Settari, A. 2008. Modeling of Geomechanics in Naturally Fractured Reservoirs. *SPE Res Eval & Eng* **11** (1): 108–118. http://dx.doi.org/10.2118/93083-PA.

Biot, M.A. 1941. General Theory of Three-Dimensional Consolidation. *J. Appl. Phys.* **12** (2): 155–164. http://dx.doi.org/10.1063/1.1712886.

Biot, M.A. and Willis, D.G. 1957. The Elastic Coefficients of the Theory of Consolidation. *J. Appl. Mech.* **24:** 594–601.

Bishop, A.W. 1959. The Principle of Effective Stress. *Teknisk Ukeblad* **106:** 859–863.

Bishop, A.W. and Donald, I. 1961. The Experimental Study of Partly Saturated Soil in the Triaxial Apparatus. Proc., 5th International Conference on Soil Mechanics & Foundation Engineering, Paris, France, 13–21.

Borja, R.I. 2006. On the Mechanical Energy and Effective Stress in Saturated and Unsaturated Porous Continua. *Int. J. Solids Struct.* **43** (6): 1764–1786. http://dx.doi.org/10.1016/j.ijsolstr.2005.04.045.

Cappa, F. and Rutqvist, J. 2011. Impact of CO_2 Geological Sequestration on the Nucleation of Earthquakes. *Geophys. Res. Lett.* **38** (17): L17313. http://dx.doi.org/10.1029/2011GL048487.

Chiaramonte, L., Zoback, M.D., Friedmann, J., et al. 2008. Seal Integrity and Feasibility of CO_2 Sequestration in the Teapot Dome EOR Pilot: Geomechanical Site Characterization. *Environ. Geol.* **54** (8): 1667–1675. http://dx.doi.org/10.1007/s00254-007-0948-7.

Coussy, O. 1995. *Mechanics of Porous Continua*. Chichester, England: John Wiley and Sons.

Coussy, O. 2004. *Poromechanics*. Chichester, England: John Wiley and Sons.

Coussy, O. 2005. Poromechanics of Freezing Materials. *J. Mech. Phys. Solids* **53** (8): 1689–1718. http://dx.doi.org/10.1016/j.jmps.2005.04.001.

Coussy, O., Eymard, R., and Lassabatére, T. 1998. Constitutive Modeling of Unsaturated Drying Deformable Materials. *J. Eng. Mech.* **124** (6): 658–667. http://dx.doi.org/10.1061/(ASCE)0733-9399(1998)124:6(658).

Dangla, P., Coussy, O., Olchizky, E., et al. 2000. Non-Linear Thermomechanical Couplings in Unsaturated Clay Barriers. Proc., 1999 IUTAM Symposium on Theoretical and Numerical Methods Continuum Mechanics of Porous Materials, University of Stuttgart, Germany, 139–144. http://dx.doi.org/10.1007/0-306-46953-7_20.

Ferronato, M., Castelletto, N., and Gambolati, G. 2010. A Fully Coupled 3-D Mixed Finite Element Model of Biot Consolidation. *J. Comput. Phys.* **229** (12): 4813–4830. http://dx.doi.org/10.1016/j.jcp.2010.03.018.

Fredlund, D.G. and Rahardjo, H. 1993a. *Soil Mechanics for Unsaturated Soils*. New York City, New York: Wiley-Interscience.

Fredlund, D.G. and Rahardjo, H. 1993b. An Overview of Unsaturated Soil Behaviour. ASCE Specialty Series on Unsaturated Soil Properties, 1–31, New York: ASCE.

Freeman, T.T., Chalaturnyk, R.J., and Bogdanov, I.I. 2009. Geomechanics of Heterogeneous Bitumen Carbonates. Presented at the SPE Reservoir Simulation Symposium, The Woodlands, Texas, 2–4 February. SPE-119151-MS. http://dx.doi.org/10.2118/119151-MS.

Gai, X. 2004. *A Coupled Geomechanics and Reservoir Flow Model on Parallel Computers*. PhD dissertation, University of Texas at Austin, Austin, Texas (August 2004).

Geertsma, J. 1957. The Effect of Fluid Pressure Decline on Volumetric Change of Porous Rocks. *Petrol. Trans. AIME* **210:** 331–340.

Gutierrez, M.S. and Lewis, R.W. 2002. Coupling of Fluid and Deformation in Underground Formations. *J. Eng. Mech.* **128** (7): 779–787. http://dx.doi.org/10.1061/(ASCE)0733-9399(2002)128:7(779).

Holtzman, R. and Juanes, R. 2011. Thermodynamic and Hydrodynamic Constraints on Overpressure Caused by Hydrate Dissociation: A Pore-Scale Model. *Geophys. Res. Lett.* **38** (14): L14308. http://dx.doi.org/10.1029/2011GL047937.

Holtzman, R., Szulczewski, M.L., and Juanes, R. 2012. Capillary Fracturing in Granular Media. *Phys. Rev. Lett.* **108** (26): 264504. http://dx.doi.org/10.1103/PhysRevLett.108.264504.

Hughes, T.J.R. 1987. *The Finite Element Method: Linear Static and Dynamic Finite Element Analysis*. Englewood Cliffs, New Jersey: Prentice-Hall.

Jain, A.K. and Juanes, R. 2009. Preferential Mode of Gas Invasion in Sediments: Grain-Scale Mechanistic Model of Coupled Multiphase Fluid Flow and Sediment Mechanics. *J. Geophys. Res.* **114** (B8): B08101. http://dx.doi.org/10.1029/2008JB006002.

Jean, L., Mainguy, M., Masson, R., et al. 2007. Accelerating the Convergence of Coupled Geomechanical-Reservoir Simulations. *Int. J. Numer. Anal. Met.* **31** (10): 1163–1181. http://dx.doi.org/10.1002/nag.576.

Jha, B. and Juanes, R. 2007. A Locally Conservative Finite Element Framework for the Simulation of Coupled Flow and Reservoir Geomechanics. *Acta Geotech.* **2** (3): 139–153. http://dx.doi.org/10.1007/s11440-007-0033-0.

Josa, A. 1988. *Un Modelo Elatoplástico Para Suelos No Saturados*. PhD dissertation, Universitat Politecnica de Catalunya, Barcelona, Spain.

Josa, A., Alonso, E.E., Lloret, A., et al. 1987. Stress-Strain Behaviour of Partially Saturated Soil. Proc., 9th European Conference on Soil Mechanics and Foundation Engineering, Adelaide, Australia, 67–71.

Khalili, N. and Khabbaz, M.H. 1998. A Unique Relationship of χ for the Determination of the Shear Strength of Unsaturated Soils. *Geotechnique* **48** (5): 681–687. http://dx.doi.org/10.1680%2fgeot.1998.48.5.681.

Kim, J., Moridis, G.J., and Rutqvist, J. 2012a. Coupled Flow and Geomechanical Analysis for Gas Production in the Prudhoe Bay Unit L-106 Well Unit C Gas Hydrate Deposit in Alaska. *J. Pet. Sci. Eng.* **92–93:** 143–157. http://dx.doi.org/10.1016/j.petrol.2012.04.012.

Kim, J., Moridis, G.J., Yang, D., and Rutqvist, J. 2012b. Numerical Studies on Two-Way Coupled Fluid Flow and Geomechanics in Hydrate Deposits. *SPE J.* **17** (2): 485–501. http://dx.doi.org/10.2118/141304-PA.

Kim, J., Tchelepi, H.A., and Juanes, R. 2011a. Stability, Accuracy and Efficiency of Sequential Methods for Coupled Flow and Geomechanics. *SPE J.* **16** (2): 249–262. http://dx.doi.org/10.2118/119084-PA.

Kim, J., Tchelepi, H.A., and Juanes, R. 2011b. Stability and Convergence of Sequential Methods for Coupled Flow and Geomechanics: Drained and Undrained Splits. *Comput. Methods Appl. Mech. Eng.* **200** (23–24): 2094–2116. http://dx.doi.org/10.1016/j.cma.2011.02.011.

Kim, J., Tchelepi, H.A., and Juanes, R. 2011c. Stability and Convergence of Sequential Methods for Coupled Flow and Geomechanics: Fixed-Stress and Fixed-Strain Splits. *Comput. Methods Appl. Mech. Eng.* **200** (13–16): 1591–1606. http://dx.doi.org/10.1016/j.cma.2010.12.022.

Kosloff, D., Scott, R., and Scranton, J. 1980. Finite Element Simulation of Wilmington Oil Field Subsidence: I. Linear Modelling. *Tectonophysics* **65** (3–4): 339–368. http://dx.doi.org/10.1016/0040-1951(80)90082-7.

Lewis, R.W., Makurat, A., and Pao, W.K.S. 2003. Fully Coupled Modelling of Seabed Subsidence and Reservoir Compaction of North Sea Oil Fields. *Hydrogeol. J.* **11** (1): 142–161. http://dx.doi.org/10.1007/s10040-002-0239-z.

Lewis, R.W. and Schrefler, B.A. 1998. *The Finite Element Method in the Static and Dynamic Deformation and Consolidation of Porous Media*, second edition. Chichester, England: Wiley.

Lewis, R.W. and Sukirman, Y. 1993a. Finite Element Modelling for Simulating the Surface Subsidence Above a Compacting Hydrocarbon Reservoir. *Int. J. Numer. Anal. Methods Geomech.* **18** (9): 619–639. http://dx.doi.org/10.1002/nag.1610180904.

Lewis, R.W. and Sukirman, Y. 1993b. Finite Element Modelling of Three-Phase Flow in Deforming Saturated Oil Reservoirs. *Int. J. Numer. Anal. Methods Geomech.* **17** (8): 577–598. http://dx.doi.org/10.1002/nag.1610170804.

Li, X., Liu, Z., and Lewis, R.W. 2005. Mixed Finite Element Method for Couple Thermo-Hydro-Mechanical Process in Poro-Elastic-Plastic Media at Large Strains. *Int. J. Numer. Meth. Eng.* **64** (5): 667–708. http://dx.doi.org/10.1002/nme.1469.

Mainguy, M., Coussy, O., and Baroghel-Bouny, V. 2001. Role of Air Pressure in Drying of Weakly Permeable Materials. *J. Eng. Mech.* **127** (6): 582–592. http://dx.doi.org/10.1061/(ASCE)0733-9399(2001)127: 6(582).

Mainguy, M. and Longuemare, P. 2002. Coupling Fluid Flow and Rock Mechanics: Formulations of the Partial Coupling Between Reservoir and Geomechanics Simulators. *Oil Gas Sci. Tech.* **57** (4): 355–367. http://dx.doi.org/10.2516/ogst:2002023.

Marsden, J.E. and Hughes, T.J.R. 1983. *Mathematical Foundations of Elasticity*. Englewood Cliffs, New Jersey: Prentice-Hall.

Maswoswe, J. 1985. *Stress Path for a Compacted Soil During Collapse due to Wetting*. PhD dissertation, Imperial College London, London, UK (May 1985).

Mayor, J., Velasco, M., and Garcia-Sineriz, J. 2007. Ventilation Experiment in the Mont Terri Underground Laboratory. *Phys. Chem. Earth* **32** (8–14): 616–628. http://dx.doi.org/10.1016/j.pce.2006.04.030.

Merle, H.A., Kentie, C.J.P., van Opstal, G.H.C., et al. 1976. The Bachaquero Study–A Composite Analysis of the Behavior of a Compaction Drive/Solution Gas Drive Reservoir. *J. Pet. Tech.* **28** (9): 1107–1114. http://dx.doi.org/10.2118/5529-PA.

Morris, J.P., Hao, Y., Foxall, W., et al. 2011. A Study of Injection-Induced Mechanical Deformation at the In Salah CO_2 Storage Project. *Int. J. Greenh. Gas Con.* **5** (2): 270–280. http://dx.doi.org/10.1016/j.ijggc.2010.10.004.

Murad, M.A. and Loula, A.F.D. 1992. Improved Accuracy in Finite Element Analysis of Biot's Consolidation Problem. *Comput. Methods Appl. Mech. Eng.* **95** (3): 359–382. http://dx.doi.org/10.1016/0045-7825(92)90193-N.

Murad, M.A. and Loula, A.F.D. 1994. On Stability and Convergence of Finite Element Approximations of Biot's Consolidation Problem. *Comput. Methods Appl. Mech. Eng.* **37** (4): 645–667. http://dx.doi.org/10.1002/nme.1620370407.

Nuth, M. and Laloui, L. 2008. Effective Stress Concept in Unsaturated Soils: Clarification and Validation of a Unified Framework. *Int. J. Numer. Anal. Methods Geomech.* **32** (7): 771–801. http://dx.doi.org/10.1002/nag.645.

Olivella, S., Gens, A., Carrera, J., et al. 1996. Numerical Formulation for a Simulator (CODE_BRIGHT) for the Coupled Analysis of Saline Media. *Eng. Comput.* **13** (7): 87–112. http://dx.doi.org/10.1108/02644409610151575.

Pao, W.K.S. and Lewis, R.W. 2002. Three Dimensional Finite Element Simulation of Three-Phase Flow in a Deforming Fissured Reservoir. *Comput. Methods Appl. Mech. Eng.* **191** (23–24): 2631–2659. http://dx.doi.org/10.1016/S0045-7825(01)00420-0.

Pao, W.K.S., Lewis, R.W., and Masters, I. 2001. A Fully Coupled Hydro-Thermo-Poro-Mechanical Model for Black Oil Reservoir Simulation. *Int. J. Numer. Anal. Methods Geomech.* **25** (12): 1229–1256. http://dx.doi.org/10.1002/nag.174.

Phillips, P.J. and Wheeler, M.F. 2007a. A Coupling of Mixed and Continuous Galerkin Finite Element Methods for Poroelasticity I: The Continuous in Time Case. *Comput. Geosci.* **11** (2): 131–144. http://dx.doi.org/10.1007/s10596-007-9045-y.

Phillips, P.J. and Wheeler, M.F. 2007b. A Coupling of Mixed and Continuous Galerkin Finite Element Methods for Poroelasticity II: The Discrete-in-Time Case. *Comput. Geosci.* **11** (2): 145–158. http://dx.doi.org/10.1007/s10596-007-9044-z.

Rutqvist, J., Birkholzer, J.T., and Tsang, C.F. 2008. Coupled Reservoir-Geomechanical Analysis of the Potential for Tensile and Shear Failure Associated with CO_2 Injection in Multilayered Reservoir-Caprock Systems. *Int. J. Rock Mech. Min. Sci.* **45** (2): 132–143. http://dx.doi.org/10.1016/j.ijrmms.2007.04.006.

Rutqvist, J., Borgesson, L., Chijimatsu, M., et al. 2001. Thermohydromechanics of Partially Saturated Geological Media: Governing Equations and Formulation of Four Finite Element Models. *Int. J. Rock Mech. Min. Sci.* **38** (1): 105–127. http://dx.doi.org/10.1016/S1365-1609(00)00068-X.

Rutqvist, J. and Moridis, G.J. 2009. Numerical Studies on the Geomechanical Stability of Hydrate-Bearing Sediments. *SPE J.* **14** (2): 267–282. http://dx.doi.org/10.2118/126129-PA.

Settari, A. and Mourits, F. 1994. Coupling of Geomechanics and Reservoir Simulation Models. In *Computer Methods and Advances in Geomechanics*, eds. H. J. Siriwardane and M. M. Zaman, 2151–2158. Balkema, Rotterdam, the Netherlands.

Settari, A. and Mourits, F. 1998. A Coupled Reservoir and Geomechanical Simulation System. *SPE J.* **3** (3): 219–226. http://dx.doi.org/10.2118/50939-PA.

Simo, J. 1991. Nonlinear Stability of the Time-Discrete Variational Problem of Evolution in Nonlinear Heat Conduction, Plasticity and Viscoplasticity. *Comput. Methods Appl. Mech. Eng.* **88** (1): 111–131. http://dx.doi.org/10.1016/0045-7825(91)90235-X.

Simo, J. and Govindjee, S. 1991. Nonlinear B-Stability and Symmetry Preserving Return Mapping Algorithms for Plasticity and Viscoplasticity. *Int. J. Numer. Anal. Methods Geomech.* **31** (1): 151–176. http://dx.doi.org/10.1002/nme.1620310109.

Sukirman, Y. and Lewis, R.W. 1993. A Finite Element Solution of a Fully Coupled Implicit Formulation for Reservoir Simulation. *Int. J. Numer. Anal. Methods Geomech.* **17** (10): 677–698. http://dx.doi.org/10.1002/nag.1610171002.

Szulczewski, M.L., MacMinn, C.W., Herzog, H.J., et al. 2012. The Lifetime of Carbon Capture and Storage as a Climate-Change Mitigation Technology. *Proc. Natl. Acad. Sci. USA.* **109** (14): 5185–5189. http://dx.doi.org/10.1073/pnas.1115347109.

Terzaghi, K., Peck, R.B., and Mesri, G. 1996. *Soil Mechanics in Engineering Practice*. New York, New York: John Wiley & Sons.

Truty, A. and Zimmermann, T. 2006. Stabilized Mixed Finite Element Formulations for Materially Nonlinear Partially Saturated Two-Phase Media. *Comput. Methods Appl. Mech. Eng.* **195** (13–16): 1517–1546. http://dx.doi.org/10.1016/j.cma.2005.05.044.

Vermeer, P.A. and Verruijt, A. 1981. An Accuracy Condition for Consolidation by Finite Elements. *Int. J. Numer. Anal. Methods Geomech.* **5** (1): 1–14. http://dx.doi.org/10.1002/nag.1610050103.

Wan, J. 2002. *Stabilized Finite Element Methods for Coupled Geomechanics and Multiphase Flow*. PhD dissertation, Stanford University, Stanford, California (November 2002).

Wan, J., Durlofsky, L.J., Hughes, T.J.R., et al. 2003. Stabilized Finite Element Methods for Coupled Geomechanics Reservoir Flow Simulations. Presented at the SPE Reservoir Simulation Symposium, Houston, Texas, 3–5 February. SPE-79694-MS. http://dx.doi.org/10.2118/79694-MS.

White, A.J. and Borja, R.I. 2008. Stabilized Low-Order Finite Elements for Coupled Solid-Deformation/Fluid-Diffusion and Their Application to Fault Zone Transients. *Comput. Methods Appl. Mech. Eng.* **197** (49–50): 4353–4366. http://dx.doi.org/10.1016/j.cma.2008.05.015.

Yin, S., Dusseault, M.B., and Rothenburg, L. 2009. Thermal Reservoir Modeling in Petroleum Geomechanics. *Int. J. Numer. Anal. Methods Geomech.* **33** (4): 449–485. http://dx.doi.org/10.1002/nag.723.

Zhang, C., Rothfuchs, T., Su K., et al. 2007. Experimental Study of the Thermo-Hydro-Mechanical Behaviour of Indurated Clays. *Phys. Chem. Earth* **32** (8–14): 957–965. http://dx.doi.org/10.1016/j.pce.2006.04.038.

Zienkiewicz, O.C., Paul, D.K., and Chan, A.H.C. 1988. Unconditionally Stable Staggered Solution Procedure for Soil-Pore Fluid Interaction Problems. *Int. J. Numer. Meth. Eng.* **26** (5): 1039–1055. http://dx.doi.org/10.1002/nme.1620260504.

Jihoon Kim is a research scientist at the Lawrence Berkeley National Laboratory, Berkeley, California. He studies geomechanical responses to geothermal energy extraction; gas production from gas hydrate, tight gas, and shale gas reservoirs; and nuclear-waste disposal. Kim also focuses on numerical modeling and simulation of coupled flow/geomechanics/geophysics processes, including hydraulic fracturing. He holds a PhD in petroleum engineering from Stanford University.

Hamdi A. Tchelepi is Professor of Energy Resources Engineering at Stanford University. He codirects the Center for

Computational Earth and Environmental Science and SUPRI-B. Tchelepi's research interests include multiscale modeling of flow in natural porous media. He holds a PhD degree in petroleum engineering from Stanford University.

Ruben Juanes is the ARCO Associate Professor in Energy Studies in the Department of Civil and Environmental Engineering at the Massachusetts Institute of Technology (MIT), Cambridge, Massachusetts. Before joining the MIT faculty in 2006, he was an acting assistant professor at Stanford University and an assistant professor at the University of Texas at Austin. Juanes works on multiphase flow through porous media and coupled flow-geomechanics. He holds a PhD degree from the University of California at Berkeley.